Synthesis of Mono-to-Multi-Layer Graphene for Transparent Electrode Applications

by

Minseok Choi

B.S. Mechanical and Aerospace Engineering
B.B.A. Business Administration
Seoul National University, 2010

SUBMITTED TO THE DEPARTMENT OF MECHANICAL ENGINEERING IN PARTIAL FULFILLMENT OF THE REQUIREMENTS FOR THE DEGREE OF

MASTER OF SCIENCE IN MECHANICAL ENGINEERING
AT THE
MASSACHUSETTS INSTITUTE OF TECHNOLOGY

JUNE 2012

Signature of Author: ____________________ ____________________
Department of Mechanical Engineering
May 11, 2012

Certified by: ____________________ ____________________
Jing Kong
Professor of Electrical Engineering and Computer Science
Thesis Supervisor

Certified by: ____________________ ____________________
Gang Chen
Professor of Mechanical Engineering
Reader

Accepted by: ____________________ ____________________
David E. Hardt
Ralph E. and Eloise F. Cross Professor of Mechanical Engineering
Chairman Department Committee on Graduate Students

Synthesis of Mono-to-Multi-Layer Graphene for Transparent Electrode Applications

by

Minseok Choi

Submitted to the Department of Mechanical Engineering
on May 11, 2012 in Partial Fulfillment of the
Requirements for the Degree of Master of Science in
Mechanical Engineering

Abstract

In this thesis, mono-to-multilayer graphene for transparent electrode applications was synthesized by Atmospheric Pressure Chemical Vapor Deposition (APCVD) and the key factors that determine the electrical and optical properties of the graphene were isolated. This work involves optimizing APCVD conditions to grow the best quality graphene for transparent electrode applications as well as explaining the underlying mechanisms behind APCVD. The effects of methane and hydrogen in the growth step were studied along with the impact of the annealing step. Growth without hydrogen was also investigated. Sheet resistance, transmittance, and mobility data with carrier concentration information were obtained and analyzed for each growth condition. This work explored a large set of APCVD conditions with focus towards the electrical and optical properties; therefore it will be greatly beneficial for researchers who seek to the high quality graphene for the transparent electrodes and other electronic applications.

Thesis Supervisor: Jing Kong
Title: Professor of Electrical Engineering and Computer Science

Reader: Gang Chen
Title: Professor of Mechanical Engineering

Table of Contents

Chapter 1. Introduction

1.1. Rise of Graphene as a Transparent Electrode

Transparent conductive films (TCF) are one of the most widely used electrical components in the world. LCD monitors, flat panel TV's, solar cells, and even touch screen contain transparent conductive electrodes. The market size of TCFs in 2012 is estimated to be \$1.63 billion[21], and will grow rapidly with the increasing importance of electrical displays in our lives. Currently, ITO controls 93% of the market[21] because of its outstanding electrical and optical properties. Commercially available ITO boasts low sheet resistance (~10Ω/□) and relatively high transmittance (~85%). However, there are several major obstacles that hinder the continued use and expansion of ITO as a transparent electrode: (i) ITO is expensive due to the high cost of indium, (ii) its supply fluctuates as market demand varies, (iii) its supply is limited by the availability of indium, (iv) it diffuses to organic layers, (v) it is not stable in presence of acid or base, (vi) it has low transmittance at near-infrared wavelengths, (vii) and it is brittle thus cannot be utilized as a flexible electrode. Thus, much research has been focused around developing other viable materials.

Graphene, which is a two-dimensional hexagonal array of carbon atoms, has emerged as a promising alternative to ITO due to its excellent electronic, optical and mechanical properties. Single-layer graphene can exhibit carrier mobility of up to $60{,}000(\mathrm{cm}^2/\mathrm{V}\cdot\mathrm{s})$, and has 97.7% transparency. In addition, graphene is chemically stable and can maintain its electrical and electronic properties even after repeated applications of mechanical stress.

To utilize its extraordinary properties, much research has been conducted on application of graphene as a transparent electrode. In 2008, Xuan Wang et al.[1] demonstrated a Dye-Sensitized Solar Cell (DSSC) device with thermally reduced graphene oxide as a transparent conductive electrode. This paper was one of the early studies on graphene-based TCFs. However, due to the low quality of the thermally reduced graphene oxide film and poorly-optimized devices, the DSSC displayed power conversion efficiency (PCE) of only 0.26%. This value is more than three times lower than the PCE of FTO implanted DSSCs (0.84%). Another paper demonstrating the use of graphene as a transparent electrode film was published in 2008. Junbo Wu et al.[2]

fabricated organic solar cells with solution-processed graphene. The reduced graphene film had sheet resistance of 100 to 500 (kΩ/□), and transparency range from 85% to 95%. The performance of the graphene device was: $J_{SC} = 2.1\, mA/cm^2$, $V_{OC} = 0.48V$, FF = 0.34, and PCE = 0.4%. On the other hand, the same device with ITO demonstrated higher performance with $J_{SC} = 2.8\, mA/cm^2$ $V_{OC} = 0.47V$, FF = 0.54, and PCE = 0.84%. The difference was mainly due to the poor sheet resistance of the solution processed graphene.

To improve upon the sheet resistance of reduced graphene electrodes, several groups created composite graphene-CNT transparent conducting films. Vincent C. Tung et al.[3] synthesized graphene-CNT nanocomposite films with sheet resistance of 240Ω/□ and 86% transmittance. The fabricated polymer solar cell with the nanocomposite transparent electrode demonstrated 0.85% power conversion efficiency. Jen-Hsien Huang et al.[4] used graphene-CNT composites to tune the work function of the transparent conducting electrode from 5.1 to3.4eV. By optimizing the condition of the TCF, PCF of up to 1.27% using inverted-architecture polymer photovoltaic devices was achieved. The sheet resistance and transmittance at optimized TCF conditions are 331Ω/□ and 65.8%.

Although solution processing has numerous advantages, Chemical Vapor Deposition (CVD) is more suitable for mass production of high quality graphene. Minhyeok Choe et al.[5] demonstrated high efficiency organic photovoltaic devices (OPVs) by utilizing multilayer graphene and a TiO_X hole-blocking layer. The PCE was comparable to that of the same device fabricated using ITO as the electrode. Recently, Xiaochang Miao et al.[6] demonstrated the highest efficiency graphene-based solar cell, with power conversion efficiency of 8.6%. To achieve this PCE, the author used single layer CVD graphene in a Schottky junction solar cell. Aside from solar cells, CVD graphene was also utilized as transparent electrode for OLEDs to improve their efficiency. Tae-Hee Han et al.[7] fabricated OLED devices with high luminous efficiencies ($37.2\, \mathrm{lmW}^{-1}$ in fluorescent OLEDs, $102.7\, \mathrm{lmW}^{-1}$ in phosphorescent OLEDs) by integrating a CVD graphene electrode. These luminous efficiencies are higher than those of ITO electrode devices. ($24.1\, \mathrm{lmW}^{-1}$ in fluorescent OLEDs, $85.6\, \mathrm{lmW}^{-1}$ in phosphorescent OLEDs) Also, a touch screen with CVD graphene electrodes was demonstrated by Sukang Bae et al.[8]

As these results demonstrate, CVD graphene is one of the most probable candidates for next generation transparent electrodes and is scalable to the industrial level. However, the vacuum system required to grow graphene through Low Pressure Chemical Vapor Deposition process (LPCVD) increases the cost of production, and decreases the throughput. Atmospheric Pressure Chemical Vapor Deposition (APCVD) is excellent alternative for LPCVD in graphene synthesis because a complex vacuum system is not necessary. In the next section, previous studies on the APCVD graphene synthesis will be discussed.

1.2. Previous Studies on APCVD Graphene Synthesis (on copper)

Sreekar Bhaviripudi et al.[9] demonstrated that synthesizing single layer graphene with high G'/G ratio is possible with APCVD. The author also proposed a simple kinetic model for both LPCVD and APCVD graphene synthesis. Moreover, the formation of large multilayer regions refuted the previously-established self-limiting behavior of copper. Libo Gao et al.[10] showed that graphene synthesis without hydrogen is also possible. The author claimed that the lower hydrogen flow rates resulted in better sheet resistance. Even though this trend may have arisen from the change in the flow rate of the dilution gas (Ar), demonstrating graphene synthesis without hydrogen is promising for monolayer graphene synthesis through APCVD.

Ivan Vlassiouk et al.[11] studied role of hydrogen in APCVD, and suggested that the hydrogen plays the dual role of a surface activator and an etching reagent. The study provided a better understanding of the behavior of hydrogen in different flow rate ranges.

Hui Bi et al.[12] fabricated the CdTe solar cells by utilizing APCVD graphene as a front electrode. The synthesized APCVD graphene had sheet resistance of 1150 Ω/□, 97.1% transmittance, and $602.4 \mathrm{cm}^2/\mathrm{V} \cdot \mathrm{s}$ carrier mobility. The sheet resistance was improved by stacking several graphene layers. With 7 layers, the sheet resistance reached as low as 220 Ω/□, but transmittance decreased to 83.7%. Using this multi-layer stacked graphene electrode, the fabricated CdTe photovoltaic devices achieved 4.17% power conversion efficiency.

1.3. Motivation and Goals

Even though there are some APCVD graphene synthesis-related papers, they focus on growth mechanisms and rarely discuss the electrical and optical properties of APCVD graphene. For electrical applications, a study that relates the growth parameters to the electrical and optical properties of synthesized graphene is necessary. If the study is able to demonstrate a clear relationship between growth parameters and graphene properties for a wide variety of synthesis conditions, it will be greatly beneficial to the graphene community and industry.

The goal of this thesis is (i) to determine the relationship between growth parameters and the properties of graphene, (ii) to explain the underlying mechanisms of those correlations, and (iii) to suggest a variety of optimized conditions for synthesis of single to multilayer graphene for transparent electrode applications.

In the near future, photovoltaic devices using optimized APCVD graphene transparent conductive electrodes will be demonstrated.

Chapter 2. Methane Controlled Single-to-Multilayer Graphene Synthesis

In this chapter, the effect of methane on the quality of synthesized graphene will be observed and discussed. Methane has been the most popular gas phase precursor in graphene synthesis since Alfonso Reina et al.[13] successfully synthesized the material via CVD. In the standard CVD process for graphene growth, a mixture of methane and hydrogen gases is introduced to a quartz tube and heated in a furnace. At high temperatures (~1000°C) the methane molecules decompose on the copper surface, forming nuclei and growing in each domain, before finally completely covering the surface of the copper. Because of the extremely low carbon solubility of copper (~0.008wt% at 1084°C), single layer graphene has been successfully synthesized via LPCVD process. However, in APCVD case, multilayer formation in some part of the graphene was observed by Sreekar Bhaviripudi et al.[9], which showed the possibility of controlled synthesis of multilayer graphene on copper. This work investigates controlling the number of graphene layers by varying methane concentration (determined by flow rate). The electrical and optical properties of the synthesized graphene were measured for each condition.

2.1. Surface Morphologies

In this section, the morphologies and corresponding optical properties of methane flow controlled multilayer graphene is presented. From the preliminary study, several representative conditions that describe the overall effect of methane on mono-to-multilayer graphene synthesis were discovered. These conditions are shown in the table 2.1 and table 2.2. In the table 2.1, there are four different steps in the APCVD process (refer to appendix for further explanation). Step I, II, III, and IV correspond to the "Ramping", "Annealing", "Growth", and "Cooling" steps respectively. Hydrogen gas is introduced during the ramping and annealing steps to get rid of copper oxide on the copper surface and enlarge grain size. After the annealing process is complete, methane, hydrogen, and argon gases are supplied for the formation of graphene. For the cooling step, the author implemented the rapid cooling method (~2.5°C/s) to prevent the possible etching of graphene by the hydrogen gas. The gas flow rates from the growth step are maintained during this step to protect the graphene sample from probable damage or degradation. The *x* and *y* are growth parameters that are investigated in this chapter. Methane flow rate (*x*) in the growth (and cooling) step is the main parameter that will be discussed throughout this chapter. Although methane flow rate is the independent variable in this chapter, three different hydrogen flow rates (*y*) are explored to generalize the discussion. The table 2.2 summarizes the tested conditions with respect to the methane and hydrogen flow rates (*x*, *y*).

Gas	**I**	**II**	**III**	**IV**
$H_2(sccm)$	160	160	y	y
$CH_4(sccm)$			x	x
$Ar(sccm)$			1000	1000

Table 2.1. The flow rates of each gas during the APCVD process

$H_2(y)$ / $CH_4(x)$	**40**	**10**	**5**
5	A1	A2	A3
3.5	B1	B2	B3
2	C1	C2	C3
1	D1	D2	D3
0.4	E1	E2	E3

Table 2.2. The gas flow rates of methane and hydrogen during the growth step (methane controlled single-to-multilayer graphene)

For each different condition, surface morphologies were observed using optical microscopy and sheet resistance, carrier mobility, and carrier concentration were measured with a 4-point probe. Further characterization (Transmittance, Raman spectroscopy) results are presented in the subsequent sections.

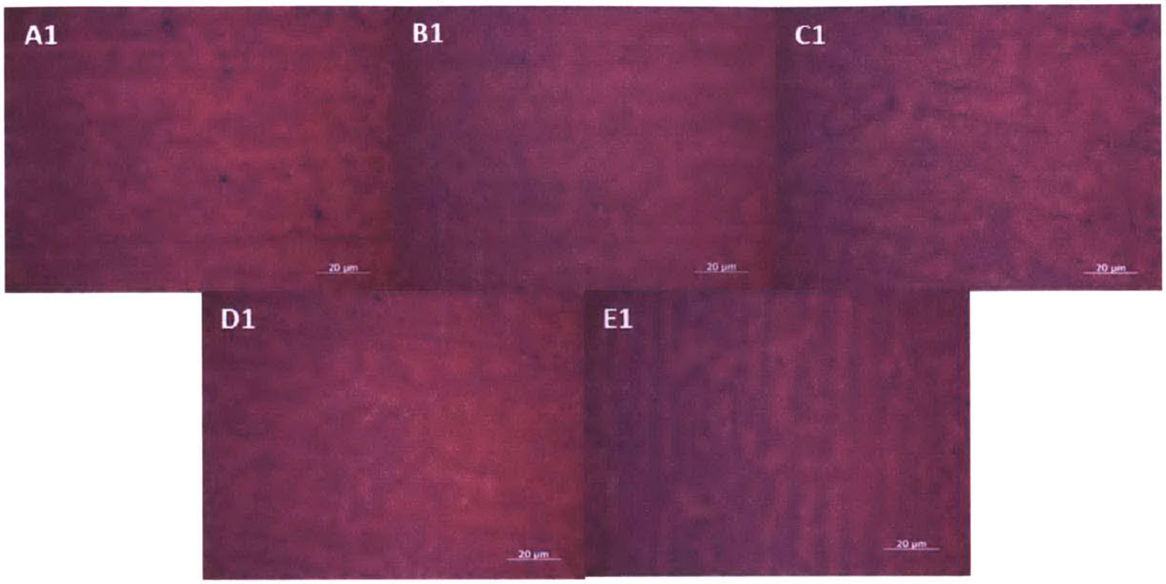

Figure 2.1. Optical Microscope Images of Methane Controlled Graphene $(\mathbf{H_2/Ar = 0.04})$
Optical microscope images for the different methane flow rates are presented. For the high hydrogen flow rate range, the multilayer coverage, distribution of multilayer, and edge regularity are similar for 1 to 5sccm methane flow rates (A1~D1). On the other hand, methane flow rates lower than 1 sccm (E1) shows\ the more regular edge shapes and clear presence of multilayers along the rolling line.

Fig. 2.1 shows the optical microscope images of methane controlled multilayer graphene samples with relatively high hydrogen flow rate $\left(\frac{H_2}{Ar} = 0.04\right)$. The multilayer graphene samples consist of two major parts: the monolayer background and the multilayer regions grown on top of the monolayer. For high hydrogen flow rates, the surface morphology of multilayer graphene samples is mostly independent of the methane flow rate except E1. For methane flow rate in the5 to 1 sccm range $\left(\frac{H_2}{CH_4} = 8 \sim 40\right)$, more than 50% of the entire monolayer surface is covered by two to three layer of graphene and the distribution of multilayer is random for the rolling line direction, and has regularity along the direction normal to the rolling line. Multilayers are concentrated near the rolling line since the active radicals fly through the surface of copper foil, preferentially landing on the valley like rolling line and forming nuclei. Multilayer regions are formed at the nuclei formation site, expand to the outer region, and stop growing when the copper foil is covered by monolayer graphene. Therefore, the multilayer regions are concentrated near the initial nucleation sites, which happen to be along the rolling lines of the copper foil.

On the other hand, the multilayer configuration of low methane flow rate sample E1 ($CH_4/H_2 = 0.01$) presents more regular edge shape compared to other samples, even though the coverage of multilayer is similar to other conditions.

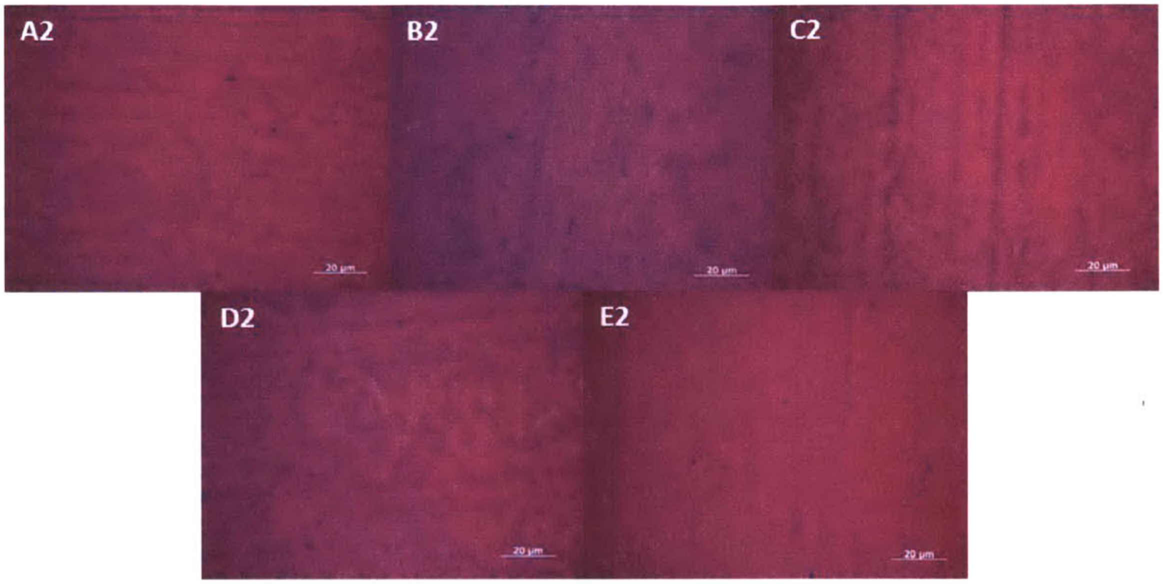

Figure 2.2. Optical Microscope Images of Methane Controlled Graphene ($H_2/Ar = 0.01$)

Fig. 2.2 shows the surface morphologies of methane controlled APCVD graphene grown in the moderate hydrogen flow environment. Noticeable decreases in multilayer coverage compared to the high hydrogen flow rate range can be observed. In addition, in the low hydrogen region ($H_2/Ar = 0.010$), lower methane flow rates result in fewer multilayer regions.

The surface configuration of methane controlled multilayer graphene in the low hydrogen flow rate region ($H_2/Ar = 0.005$) is shown in Fig. 2.3. Interestingly, the multilayer coverage of the condition A3 is largest among the conditions in this section. Changes in the area of multilayer region are much more dramatic in this series, and E3 shows clean monolayer graphene with some bilayer islands. This clearly demonstrates that the surface limiting characteristic of copper foil is less suitable for APCVD than LPCVD. In addition, the results show that control of multilayer formation is achievable by tuning the methane flow rate.

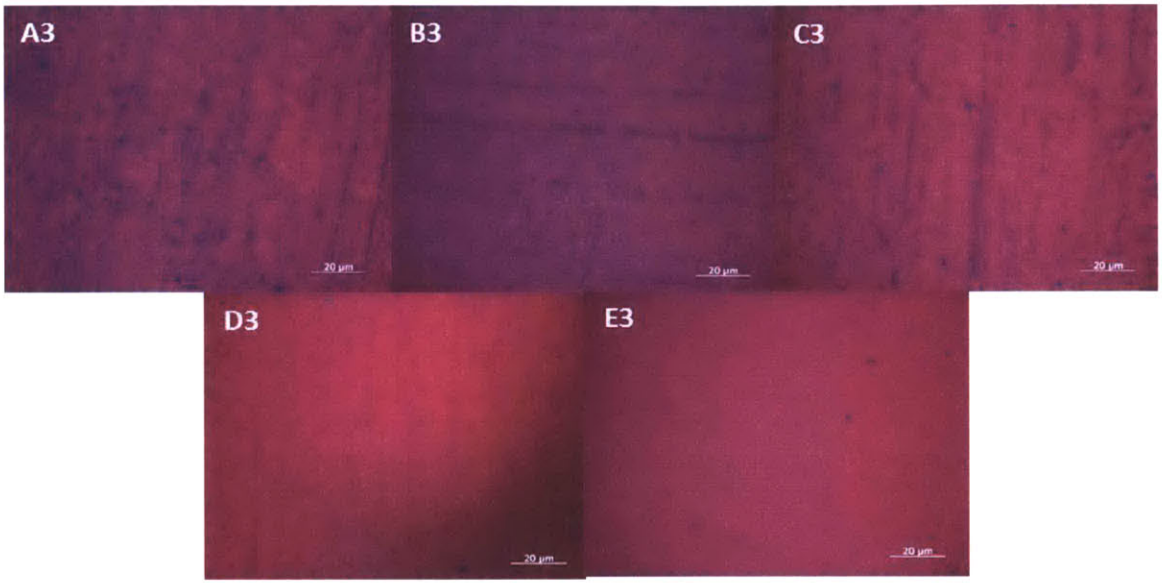

Figure 2.3. Optical Microscope Images of Methane Controlled Graphene $(H_2/Ar = 0.005)$

To advance the possibility of using APCVD graphene as a transparent electrode in practice, further characterization and analysis on the material properties should be conducted. Sheet resistance, optical transparency, mobility and corresponding carrier concentration measurement were performed and the results are shown in the following sections.

2.2. Dependence of Sheet Resistance on Methane Flow Rate

For the transparent electrode applications, sheet resistance and transmittance are the two most important parameters. To minimize the energy loss of bulk devices, low sheet resistance is required for the transparent conductive films. In this section, the effects of methane flow rate on sheet resistance for different hydrogen flow rates are presented.

To reliably measure sheet resistance values of synthesize graphene samples, 5 samples were transferred for each of condition, the sheet resistance data was extracted, and mean and standard deviation were calculated. Cracking, contamination by chemicals, folding of the film, etc. may occur during the transfer step and can affect the resulting sheet resistance. By averaging across many samples, reliable resistance data independent of transfer abnormalities can be obtained.

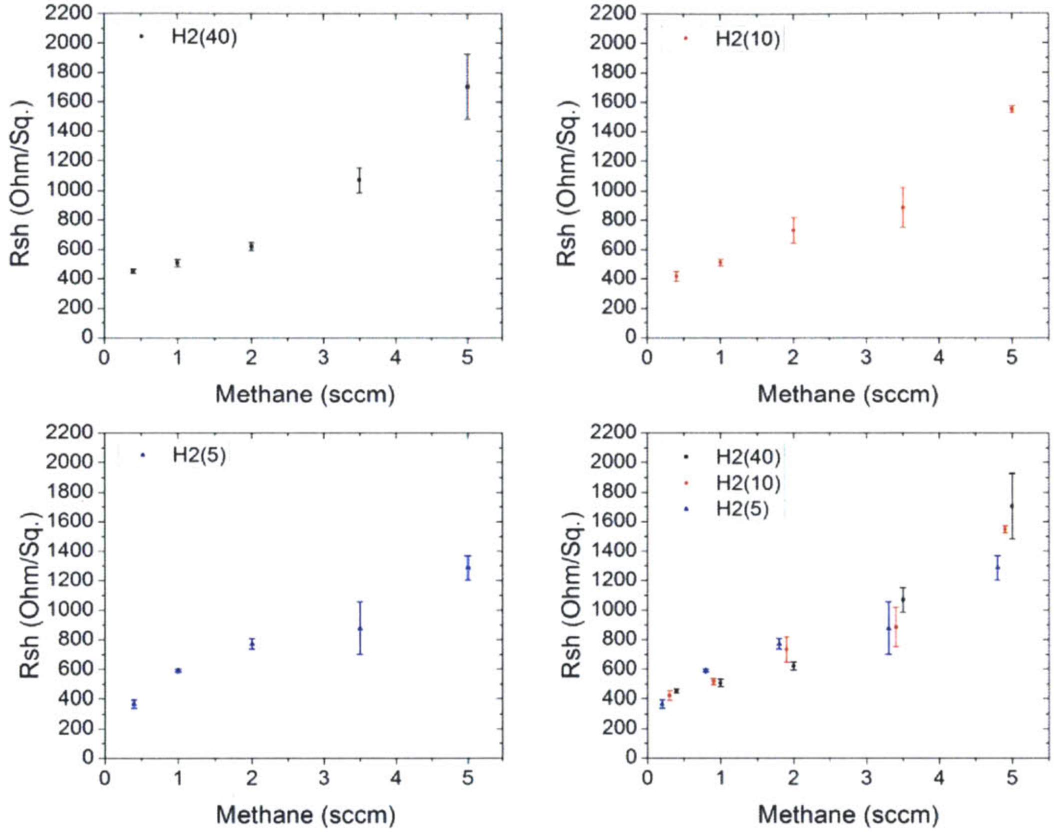

Figure 2.4. Sheet Resistance vs. Methane flow rate for Methane Controlled Multilayer Graphene

Fig. 2.4 illustrates the dependence of sheet resistance on methane flow rate in multilayer graphene. There is clear trend for the methane controlled single-to-multilayer graphene. As the methane flow rate rises, the sheet resistance of synthesized graphene increases. On the other hand, changes in the hydrogen flow rate do not have major impact on the sheet resistance. These phenomena are related to the defect density over the synthesized graphene sheet and will be discussed in the subsequent sections.

2.3. Optical Properties

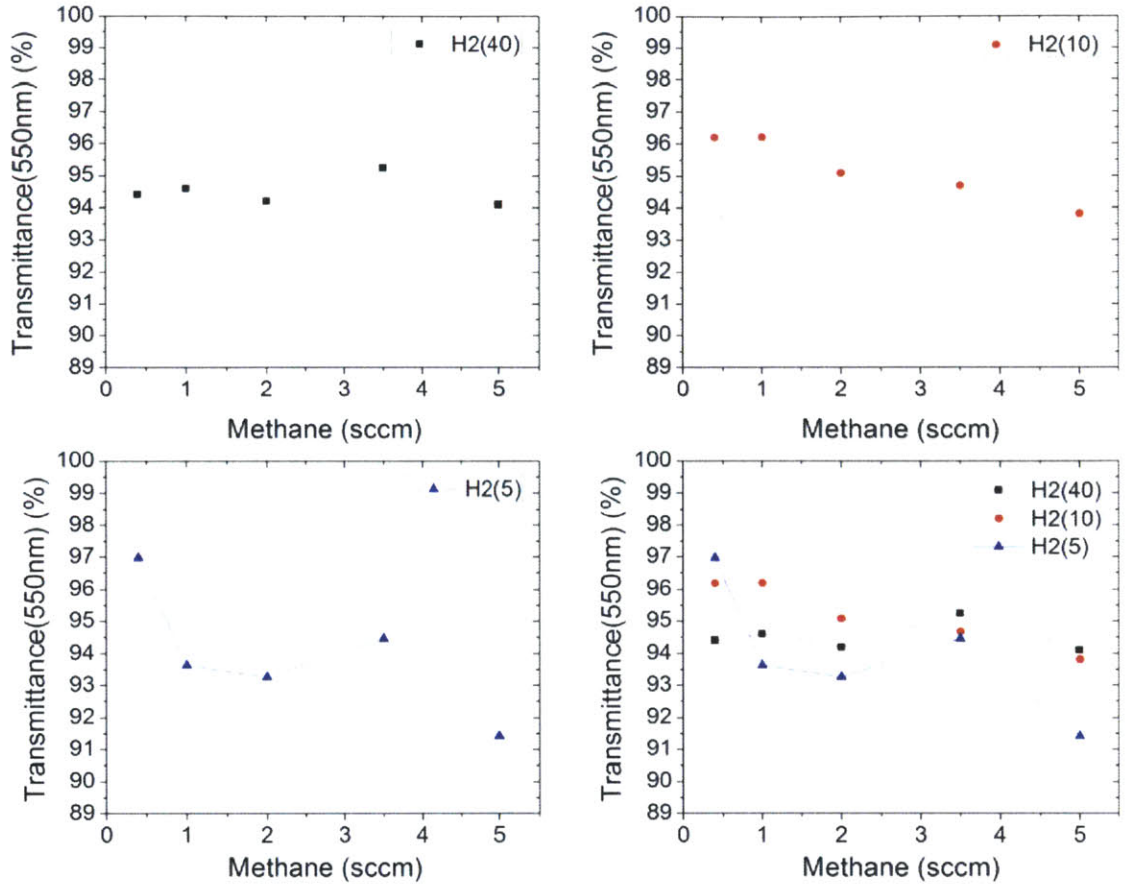

Figure 2.5. Transmittance vs. methane flow rate

Fig. 2.5 shows the transmittance data of methane controlled single-to-multilayer graphene and they represent the optical properties of synthesized graphene. Since the absorbance of graphene increases linearly with respect to the number of layers, the transmittance is directly related to the surface morphology. More specifically, the average number of layer determines the transmittance of the synthesized graphene. Fig. 2.5 represents the transmittance data with respect to the methane flow rate in the growth step. In the high hydrogen flow rate region (H2/Ar = 0.040), the transmittance shows no trend over the different methane flow rates. On the other hand, the transmittance of the graphene diminishes as the methane flow rate increases when the hydrogen flow rate is low or moderate. The lower the hydrogen flow rate, the steeper the slope of the transmittance with respect to the methane flow rate. This is related to the surface activation by hydrogen.

2.4. Carrier Mobility

Fig. 2.6-2.9 presents the carrier mobility data with respect to the methane flow rate. The carrier concentrations are displayed in parallel because the mobility is affected by carrier concentration. The carrier mobility of methane controlled graphene is inversely related to the methane flow rate; in other words, carrier mobility decreases as the methane flow rate increases. Similar to the author's observation in sheet resistance, the carrier mobility data shows similar values at each methane flow rate, irrespective of the hydrogen flow rate. (In fact, the electrical, optical properties and surface morphology changes when the hydrogen flow rate increase further ($H_2/Ar \sim 0.10$). This result is not included in here.) In the Fig. 2.9, the carrier mobility data show some samples that deviate from the global trend (CH_4 = 3.5 sccm conditions). These samples were transferred with a different batch, so it is likely that variations in the transfer step led to the variation in the electrical and optical properties. Especially, the carrier concentrations of these samples are much lower than those of other graphene samples due to longer rinse time. Considering the effect of carrier concentration on the electrical properties, the carrier mobility of the methane controlled single-to-multilayer graphene shows a clear inverse relationship with the methane flow rate.

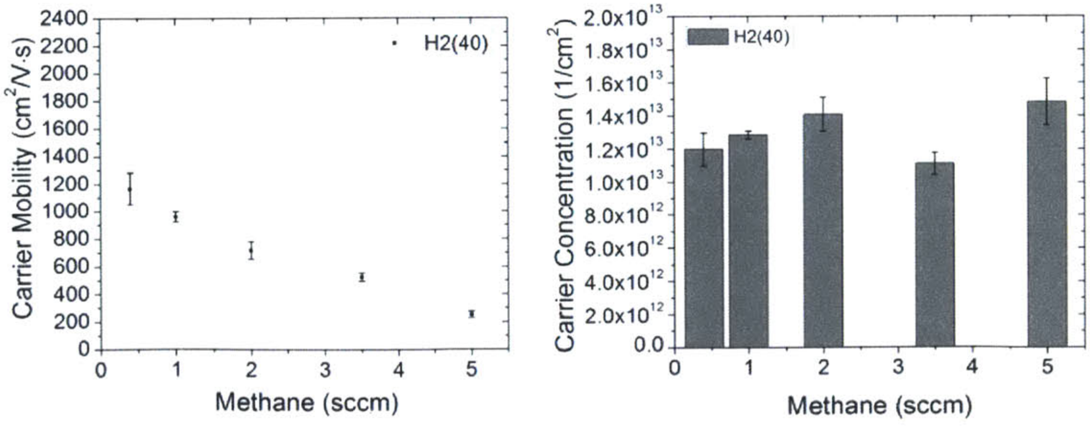

Figure 2.6. Carrier Mobility of the Methane Controlled Single-to-Multilayer Graphene (H2/Ar = 0.040)

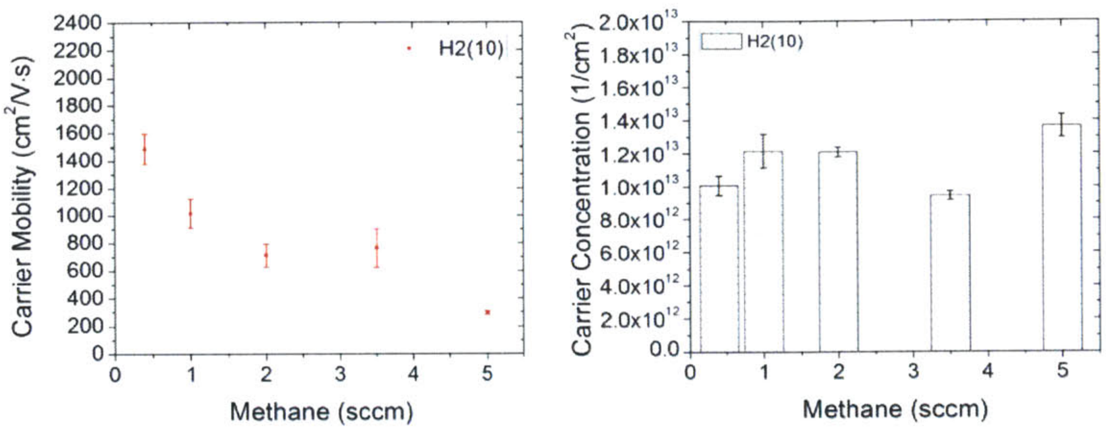

Figure 2.7. Carrier Mobility of the Methane Controlled Single-to-Multilayer Graphene (H2/Ar = 0.010)

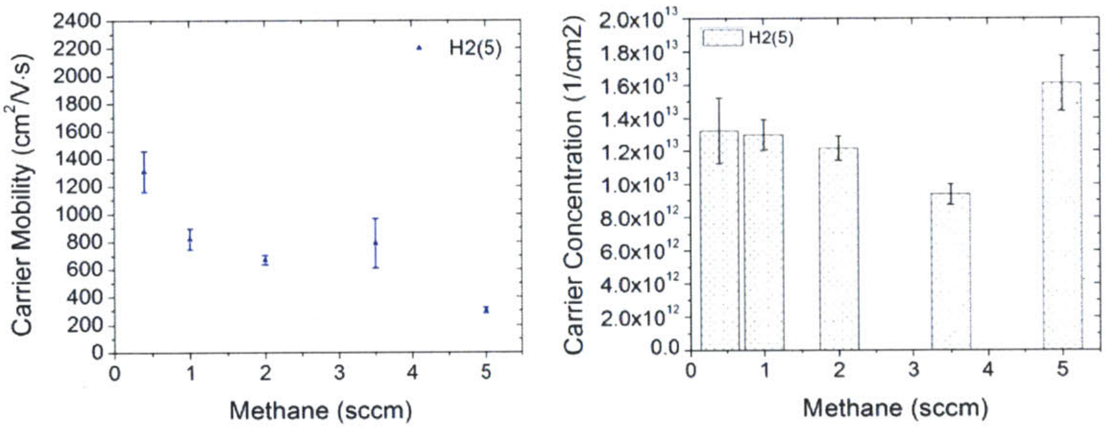

Figure 2.8. Carrier Mobility of the Methane Controlled Single-to-Multilayer Graphene (H2/Ar = 0.005)

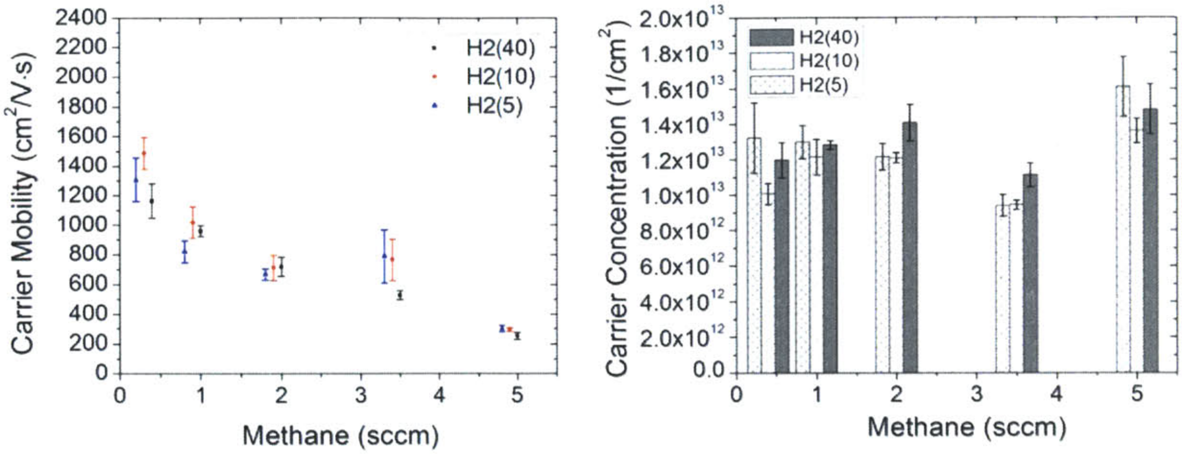

Figure 2.9. Carrier Mobility of the Methane Controlled Single-to-Multilayer Graphene

2.5. Quality of Synthesized Graphene as a Transparent Electrode

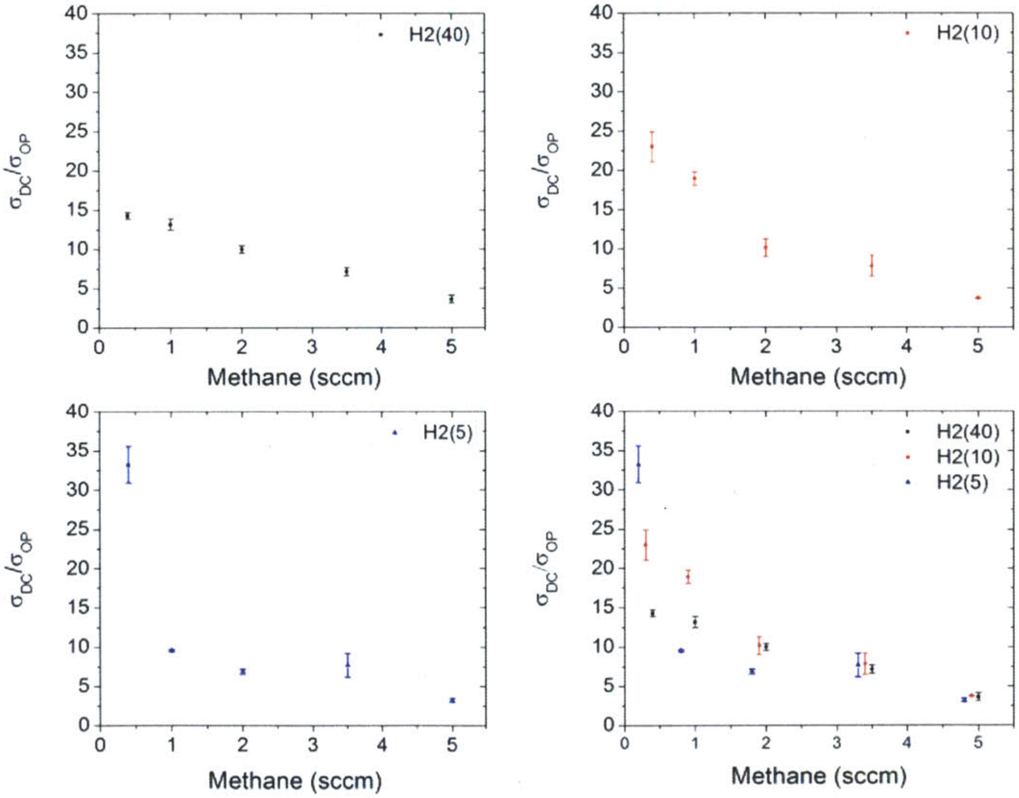

Figure 2.10. The DC to optical conductivity ratio of methane controlled single-to-multilayer graphene

To evaluate the effectiveness of the synthesized graphene samples as a transparent electrode, a metric that factors in sheet resistance and transmittance is required. For a precise evaluation, the electrical model of the system (i.e. photovoltaic device, LED display) is needed. The author will build up the model for each application in the near future. For now, we can evaluate as grown graphene with the variables that other works suggest. Sukanta De et al[14] suggested the DC-to-optical conductivity ratio as the metric for the transparent electrodes. The relationship between the parameter, the sheet resistance and transmittance can be expressed by the following equations.

$$\mathrm{R_s} = (\sigma_{\mathrm{DC}}\mathrm{t})^{-1}$$

$$\mathrm{T} = \left(1 + \frac{\mathrm{Z_0}}{2}\sigma_{\mathrm{OP}}\mathrm{t}\right)^{-2}$$

$$\mathrm{T} = \left(1 + \frac{\mathrm{Z_0}}{2\mathrm{R_s}}\frac{\sigma_{\mathrm{OP}}}{\sigma_{\mathrm{DC}}}\right)^{-2}$$

$$\frac{\sigma_{\mathrm{DC}}}{\sigma_{\mathrm{OP}}} = \frac{\mathrm{Z_0}}{2\mathrm{R_s}}\left(\frac{1}{\mathrm{T}^{-\frac{1}{2}} - 1}\right)$$

σ_{DC}, σ_{OP}, $\mathrm{R_s}$, T, t, and $\mathrm{Z_0}$ are DC conductivity, optical conductivity, sheet resistance, transmittance, thickness, and impedance of free space respectively. The DC to optical conductivity ratio $\left(\frac{\sigma_{\mathrm{DC}}}{\sigma_{\mathrm{OP}}}\right)$ takes both sheet resistance and the transmittance into account. Specifically, the ratio increases as the sheet resistance decreases and the transmittance increases. On the other hand, Siegfried Eigler suggested the conductivity of transparency, which utilizes Bouguer-Lambert law. The definition of the parameter is as shown below.

$$\sigma_{\mathrm{gt}} = \frac{1}{\rho_{sample} \cdot d_{ideal}}$$

$$-\log\left(\frac{I}{I_0}\right) = \varepsilon_{\mathrm{graphene}} d$$

$$\mathrm{d_{ideal}} = -\frac{\log\left(\frac{I}{I_0}\right)}{\varepsilon_{\mathrm{graphene}}}$$

$$\varepsilon_{\text{graphene}} = -\frac{\log\left(\frac{I}{I_0}\right)}{d_{graphite}} = -\frac{\log\left(\frac{97.7\%}{100\%}\right)}{3.35 \times 10^{-8} cm} = 301{,}655\ \text{cm}^{-1}$$

$$\sigma_{\text{gt}} = \frac{\varepsilon_{\text{graphene}}}{-\log\left(\frac{I}{I_0}\right)\rho_{sample}} = \frac{301{,}655\ \text{cm}^{-1}}{-\log\left(\frac{I}{100\%}\right)\rho_{sample}}$$

I, ρ_{sample}, and σ_{gt} are transmittance, sheet resistance, and conductivity of transparency respectively.

Both the DC to optical conductivity ratio and the conductivity of transparency are highly correlated with some constant for the transmittance range of the synthesized graphene. Therefore, the author decided to use the DC to optical conductivity as the parameter to evaluate the graphene as the transparent conductive film.

The DC to optical conductivity ratio data for the methane controlled single-to-multilayer graphene is presented in Fig. 2.10. This metric greatly improves as methane flow rate decreases. In the high methane flow rate region ($CH_4/Ar > 0.002$), the ratios for the three different hydrogen flow rate regions are similar. On the other hand, in case of low methane flow rate region ($CH_4/Ar < 0.001$), the ratio increases as the hydrogen flow rate decreases.

2.6. Raman Mapping

Fig. 2.11 is Raman mapping data taken for three different methane flow rates (CH_4 = 5, 2, 0.4 sccm for A1, C1, E1 respectively). The hydrogen flow rate for these conditions is 40 sccm. The author chose the conditions in the high hydrogen flow rate range ($H_2/Ar = 0.040$), because the surface morphologies of these conditions are very similar. By doing so, the effects of multilayer and the surface morphology are excluded. Raman mapping data were taken from the regions that have similar morphologies (ex. multilayer to single layer ratio) for three different conditions. From the G'/G ratio maps which are on the right side of the Fig. 2.11, one is able to confirm this statement. Since the D/G ratio represents the defects in the graphene sample, the distribution of defects over the graphene sheet can be measured by the D/G ratio map. The three images on the left side (Fig. 2.11) present the defect distributions resulting from those three different methane flow rates. It is clear that the defect density diminishes as the methane flow rate decreases. The relationship between the methane flow rate, defect density, and the electrical properties is discussed in the following section.

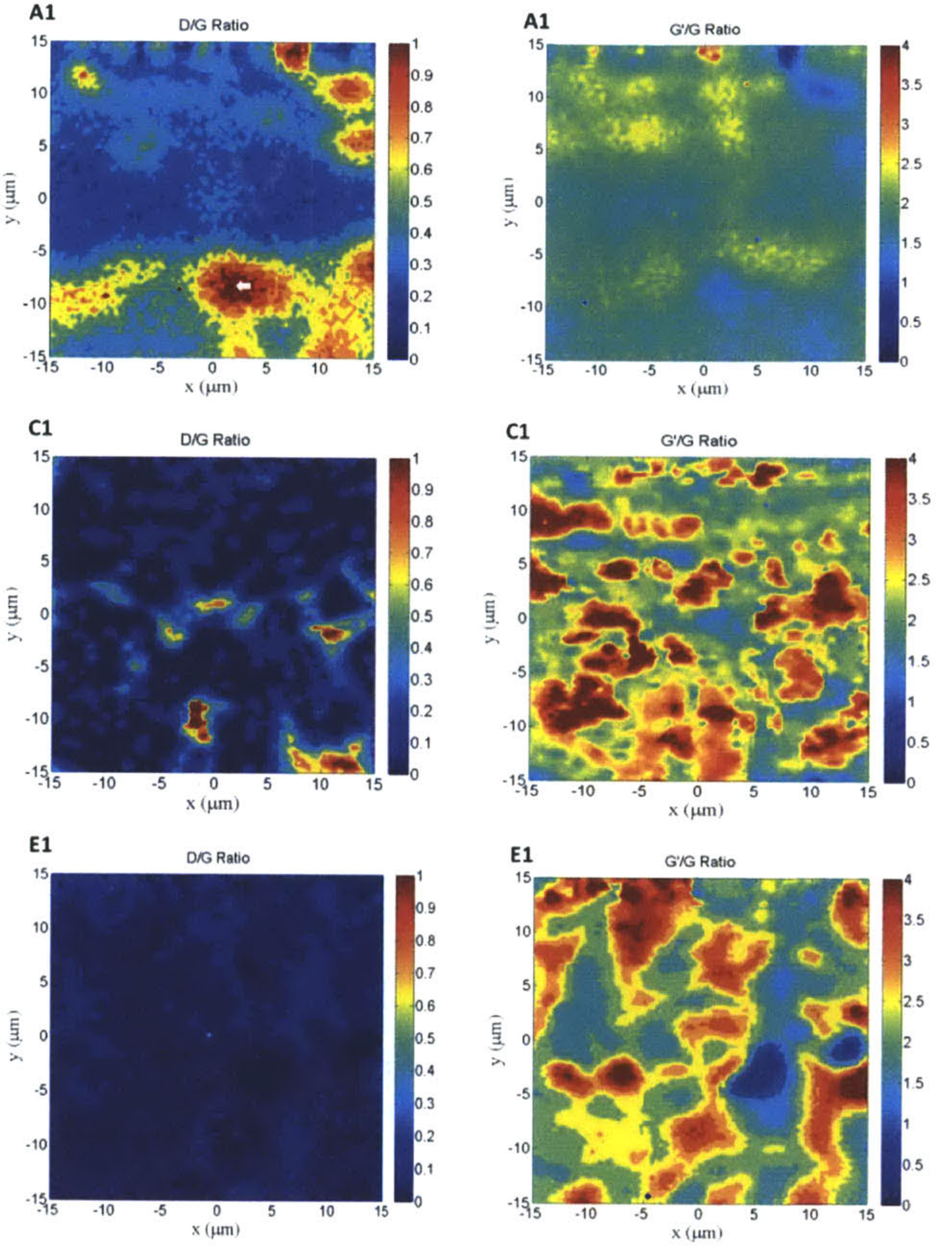

Figure 2.11. Raman mapping data of methane controlled single-to-multilayer graphene The white arrow in A1 indicates high D/G ratio island region.

2.7. Discussion

(1) Surface morphology and transmittance of the methane controlled multilayer graphene

When the concentration of hydrogen gas is higher than a certain value ($H_2/Ar\sim0.04$), the shape and coverage of multilayer regions do not change for a large range of methane flow rates ($CH_4/Ar = 0.001\sim0.005$). However, if the methane flow rate decreases further to 0.4 sccm ($CH_4/Ar = 0.0004$) the edges of multilayer graphene become more regular. To explain why these observations take place, we need to understand the mechanism of graphene synthesis in CVD system.

Sreekar Bhaviripudi et al.[9] suggested a six-step model for the graphene synthesis.

(i) Carbon species diffuse into the boundary layer and arrive at the surface.
(ii) The species are absorbed into the catalyst (copper)
(iii) The absorbed reactants are changed to the active carbon radical
(iv) The active carbon radical diffuse to the surface and form the graphene lattice
(v) The inactive species desorbed out of the catalyst
(vi) The inactive species diffuse away from the surfaces and flow downstream.

In addition to Sreekar Bhaviripudi's explanation of the CVD process, Ivan Vlassiouk et al.[11] observed the dual role of hydrogen as a surface activator and an etching agent. The authors claimed that hydrogen acts as a surface activator when its partial pressure is low, and as an etching reagent when its partial pressure is high.

The author claims that the carbon species are activated near the boundary layer region when the partial pressure of the methane is very high ($CH_4/Ar\sim0.08$, hydrogen-excluded growth case). The thick layer of graphene with high D/G ratio is observed in case of high methane and hydrogen flow rate, which lends credence to this hypothesis. Even though copper has extremely low carbon solubility, the methane may dissociate in the bulk gas flow and form the amorphous carbon on the copper and graphene surfaces.

With these growth mechanisms, variations in surface morphology over different methane flow rates are understandable. For the high hydrogen flow rate condition (H2/Ar > 0.04) the copper surface is fully activated, and the active carbon species are readily created to form multilayer graphene. Since the surface is fully activated by the absorbed hydrogen radical, the nucleation and the growth of the multilayer graphene is rapid and the coverage of multilayer is high. In the low methane flow rate ($CH_4/Ar < 0.001$) the shape of multilayer is more regular and becomes polygonal. This is because hydrogen molecules etch away the weak bonds of the synthesized graphene. The local concentration of hydrogen on the surface is high with respect to the concentration of carbon radicals so the etching effect is dramatic.

On the other hand, for the moderate and low hydrogen flow rate condition ($H_2/Ar < 0.01$), multilayer coverage heavily depends on the methane flow rate. The lower the methane flow rate, the lower the area coverage of multilayer regions. In this range of hydrogen flow rate, the surface activation for multilayer graphene synthesis is not enough to compensate for the shortage in carbon sources. The shortage in active carbon source increases as the methane flow rate decreases.

These trends are observed in the transmittance data measured at 550 nm wavelength. It is well known that the absorbance increases linearly with the number of graphene layers (2.3%/layer). Thus, the absorbance represents the average number of layers in the area where transmittance is measured. Fig. 2.5 shows that methane dependence of transmittance increases for the moderate and low hydrogen flow rate ranges. The slope of transmittance graph with respect to the methane flow rate increases, due to the shortage of surface activator (hydrogen).

(2) Sheet Resistance and mobility

The sheet resistance and mobility of graphene mainly depends on the defect density, domain size, impurities, and carrier concentration. Also, the damage to the graphene during the transfer process has detrimental effects on the electrical properties. The carrier concentration depends on the transfer and post-annealing steps which results in the variations in sheet resistance and mobility. To keep the extrinsic factors constant, and measure the intrinsic values more reliably, the author takes two precautions. First, the graphene was rinsed thoroughly, after the HCl treatment, for more than 4 hours. This mitigates the effects of the doping from the chemicals used during the transfer. Second, the electrical properties of graphene were measured 6~7 days after the post annealing step was done. Normally, graphene is doped by the underlying substrate during the annealing step, which affects the sheet resistance and carrier mobility. Even though lower sheet resistance is preferred for transparent electrode applications, waiting 6~7 days allows for more reliable and time-independent measurements. This doping effect decreases in large amount just after the post annealing step, and is stabilized after 6~7 days later.

In case of a 2D material, the sheet resistance is related to the carrier concentration and mobility by the following equation.

$$\mathrm{R_s} = \frac{1}{ne\mu}$$

From Matthiessen's Rule, the mobility can be decomposed into several independent factors as follows.

$$\frac{1}{\mu} = \frac{1}{\mu_{impurities}} + \frac{1}{\mu_{lattice}} + \frac{1}{\mu_{defects}} + \cdots$$

By combining these two equations, the relationship between the sheet resistance and the material related factors such as impurities, defect, and etc. can be expressed as:

$$\mathrm{R_s} = \frac{1}{ne\mu} = \frac{1}{ne}\left(\frac{1}{\mu_{impurities}} + \frac{1}{\mu_{lattice}} + \frac{1}{\mu_{defects}} + \cdots\right)$$

Domain size, defect density, and chemical residues impact the sheet resistance of synthesized graphene. Domain size, defect density, and concentration of residual chemicals are related to $\frac{1}{\mu_{lattice}}$, $\frac{1}{\mu_{defects}}$, and $\frac{1}{\mu_{impurities}}$ respectively.

Fig. 2.4 reveals the clear dependence of sheet resistance on the methane flow rate for methane controlled multilayer graphene. The sheet resistance decreases exponentially as methane flow rate decreases. Among three major factors, the defect density dominates this exponential trend for methane controlled graphene.

From the Raman mapping data (Fig 2.11), author could figure out the distribution of defects over the graphene sheet for different conditions. Those A1, C1, and E1 samples are synthesized in high hydrogen flow rate condition (H_2/Ar = 0.04), and had varying methane flow rates during the growth step (CH_4/Ar: 0.005(A1), 0.002(C1), 0.0004(E1)). The author chose high hydrogen conditions, since the surface morphologies of the synthesized graphene samples are similar in this range. Raman mapping data of these samples are able to prove that the quality of graphene varies even with similar surface morphologies.

In Fig. 2.11, the D/G ratio of over the $30\mu m \times 30\mu m$ area presents the distribution of defects in the sample. When the methane flow rate is high (A1), overall D/G ratio is larger compared to lower methane flow rate conditions (C1, E1). In addition, there are several small regions with high D/G ratio ($I_D/I_G > 0.8$, the white arrow indicates one of those areas) and low G'/G ratio in the sample A1 that are close to amorphous carbon. As the methane flow rate decreases, the overall D/G ratio diminishes, and the numbers and area percentages of high D/G ratio islands shrink. For the lowest methane flow rate condition (E1: $CH_4/Ar = 0.0004$), D/G ratio is much more uniform over the scanned area, the average D/G ratio is lowest among the tested conditions, and there are no amorphous carbon islands. From these observations, it is natural to conclude that the defect density becomes lower as methane flow rate decreases. When the methane flow rate is high, more methane molecules diffuse into the boundary layer and are decomposed into the active carbon species on the copper surface. Since the concentration of active carbon species is large, the neat crystalline structure of graphene on copper is not formed and both sp^2 and sp^3 bonds are created. Similarly, more defects are created in the graphene sheet because of the rapid reaction. (As Sreekar Bhaviripudi et al.[9] suggested, the surface reaction rate is dependent on the concentration of active carbon species.) Thus, graphene that is synthesized in the high methane flow rate condition has more defects which results in the lower $\mu_{defects}$. In case of methane controlled single-to-multilayer graphene, small $\mu_{defects}$ is the main factor that degrades mobility and sheet resistance. This is affirmed by the observation that the mobility and sheet resistance data shows no significant difference between various hydrogen flow rate regions. (The domain size and nucleation density depends on the methane to hydrogen flow rate ratio.[9][15] This means that the domain size does not have huge impact on the mobility and sheet resistance compare to the defect density in case of methane controlled single-to-multilayer gaphene. The effect of domain size will be shown in the hydrogen controlled single-to-multilayer graphene.) Also, Matthiessen's Rule implies that the lowest mobility factor dominates the total mobility which in this case is defect density. Thus the lower the methane flow rate, the lower the defect density and therefore, the smaller the sheet resistance.

Fig. 2.9 illustrates the decaying carrier mobility when methane flow rate increases. As discussed above, this is due to the increased defect density of the synthesized graphene. However, the carrier concentration should be considered to understand the behavior of carrier mobility with respect to the methane flow rate because carrier mobility is affected by carrier concentration. Again, Fig. 2.9 shows the carrier concentration of methane controlled graphene. The trend for carrier mobility is very clear except the graphene synthesized with 3.5sccm of methane flow. These samples were transferred in a different batch and rinsed in DI water for longer. Thus, they have lower carrier concentrations compare to other samples. In case of lower carrier concentration samples, carrier mobility is higher since ionized impurity scattering takes place less frequently. If we consider the effect of carrier concentration on the mobility, the decaying trend of carrier mobility with respect to the increasing methane flow rate is evident.

(3) Evaluation of Methane Controlled Single-to-Multilayer Graphene as a Transparent Electrode

The DC to optical conductivity ratio, σ_{DC}/σ_{OP}, provides rough figure of merit for transparent conductive electrodes. In case of methane controlled single-to-multilayer graphene, the sheet resistance decreases and transmittance increases, as the methane flow rate decreases. From the following equations, it is clear that the DC conductivity is inversely related to the sheet resistance, and the optical conductivity has negative relationship with transmittance.

$$R_s = (\sigma_{DC} t)^{-1}$$

$$T = \left(1 + \frac{Z_0}{2}\sigma_{OP} t\right)^{-2}$$

Therefore, the DC to optical conductivity ratio is improved as the methane flow rate decreases. In case of methane controlled single-to-multilayer graphene, the lower methane flow rate, the better the quality of graphene as a transparent conductive film.

From the Fig. 2.10, one is readily able to confirm this trend over 15 different conditions. The change of the conductivity ratio with respect to the methane flow rate is greater for lower hydrogen flow rates. This is because the sheet resistance values of different hydrogen flow rate regions are similar to each other but the change in the transmittance with respect to the methane flow rate is larger for the lower hydrogen conditions as the author discussed above. Roughly, the DC to optical conductivity ratio becomes higher than 11 when methane flow rate is lower than 1 sccm ($CH_4/Ar = 0.001$). The ratio reaches as high as 33.25 (on average) for single layer graphene with bilayer islands. Even though the single layer graphene shows the better conductivity ratio, multilayer graphene has certain advantages for TCF applications. Multilayer graphene is much more robust than the single layer graphene which minimizes the effects of damage accumulated during the fabrication process. In addition, the DC to optical conductivity ratio could exaggerate the importance of transmittance over the sheet resistance. The relative importance of the two parameters can be more precisely evaluated given an application-specific model.

In this chapter, the author found that one can improve the electrical, and optical properties of graphene by decreasing the methane flow rate. Also, the author noticed that the number of graphene layers can be also controlled by varying hydrogen flow; when the conditions over different hydrogen flow rate regions while kept the methane flow rate as low as possible (CH_4/Ar = 0.0004) were compared. Since the mass flow controller cannot control the flow rate less than 0.4 sccm, the author decided to use diluted methane (100ppm) for the hydrogen controlled single-to-multilayer graphene synthesis study. The hydrogen controlled single-to-multilayer graphene will be discussed in the next chapter.

Chapter 3. Control the Number of Layers with Hydrogen

In chapter 2, we learned that decreasing methane flow rate lowers defect density, which leads to the higher quality of graphene. Moreover, the change in morphology by varying the hydrogen flow is observed in chapter 2. Therefore, in this chapter, the author controls the number of layers with hydrogen by keeping the methane concentration low (CH4/Ar = 100 ppm, This concentration of diluted methane is suitable to the hydrogen controlled single-to-multilayer study because if one chooses the diluted methane with lower methane concentration, the synthesized graphene may not be completed at high hydrogen flow rate region.) By doing so, the control over the number of graphene layers is possible while maintaining the desirable electrical properties of graphene. The table 3.1 shows the overall schematic of hydrogen controlled graphene synthesis study and table 3.2 presents the specific hydrogen flow conditions for characterization. In this chapter, hydrogen flow rate (x) in the growth (and cooling) step is the independent variable. And the tested hydrogen flow rates are shown in the table 3.2. Each different condition is named in the table 3.2, and is presented on the optical microscope images.

The range of hydrogen flow rate is much wider than that of the methane flow rate in the methane controlled graphene synthesis study. This is because the hydrogen does not have detrimental effect on the defect density of the synthesized graphene, but methane does. Starting from the surface morphologies, the properties and underlying mechanisms are shown in the following sections.

Gas	I	II	III	IV
$\mathbf{H_2}$ **(*sccm*)**	160	160	x	x
Ar − a (sccm)	0	0	1000	1000

Table 3.1. The gas flow rates of hydrogen and diluted methane during APCVD process

$H_2(sccm)$	Sample
1.2	K
5	J
10	I
20	H
40	G
60	F

Table 3.2. Various hydrogen flow rates during the growth step for hydrogen controlled single-to-multilayer graphene

3.1. Surface Morphologies

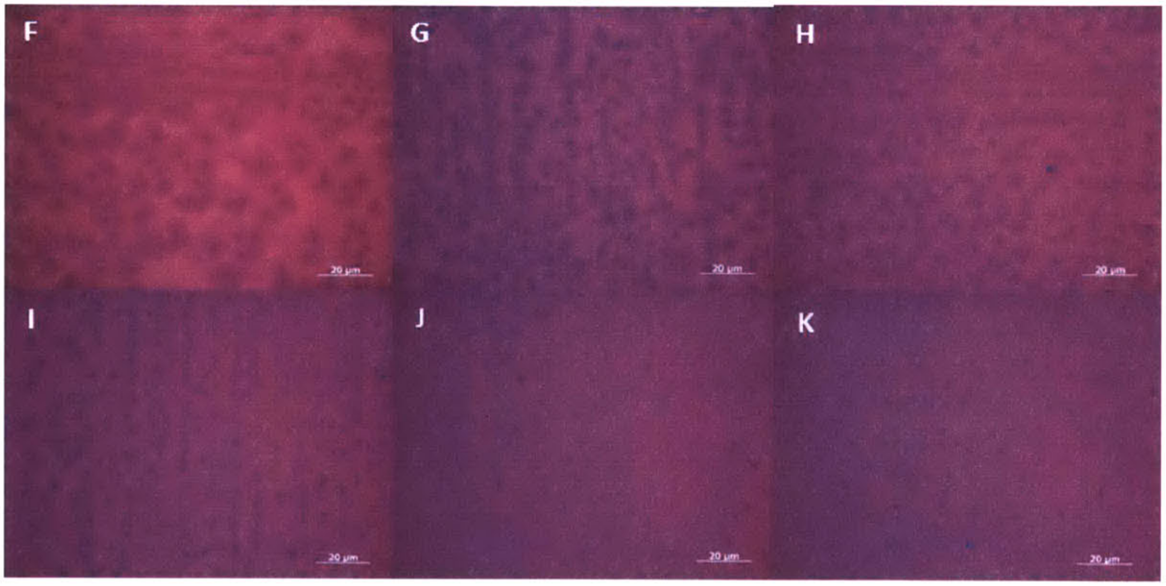

Figure 3.1. The optical microscope images of the hydrogen controlled single-to-multilayer graphene samples

The surface morphologies of hydrogen controlled graphene are shown in the Fig. 3.1. When the hydrogen flow rate is lower than critical point ($H_2/Ar < 0.040$), the average number of layers shrinks as the hydrogen flow rate decreases. As hydrogen flow rate becomes less than 5 sccm (H2/Ar < 0.005), single layer graphene with small bilayer islands is achieved. Also the thicker graphene is readily synthesized by increasing the hydrogen flow rate. On the other hand, when the hydrogen flow rate is larger than the critical point ($H_2/Ar > 0.060$), a lot of openings are observed in the graphene. In fact, it is hard to visually determine whether the brighter regions in the sample F are openings or monolayer background. This is confirmed by Raman mapping data presented in the Fig. 3.3. The G' and G peak intensities are extracted from the data and normalized by the silicon peak. By comparing the optical microscope image on the left side to Raman mapping data, we can easily confirm that the brighter regions are openings because the peak intensities in those regions are zero.

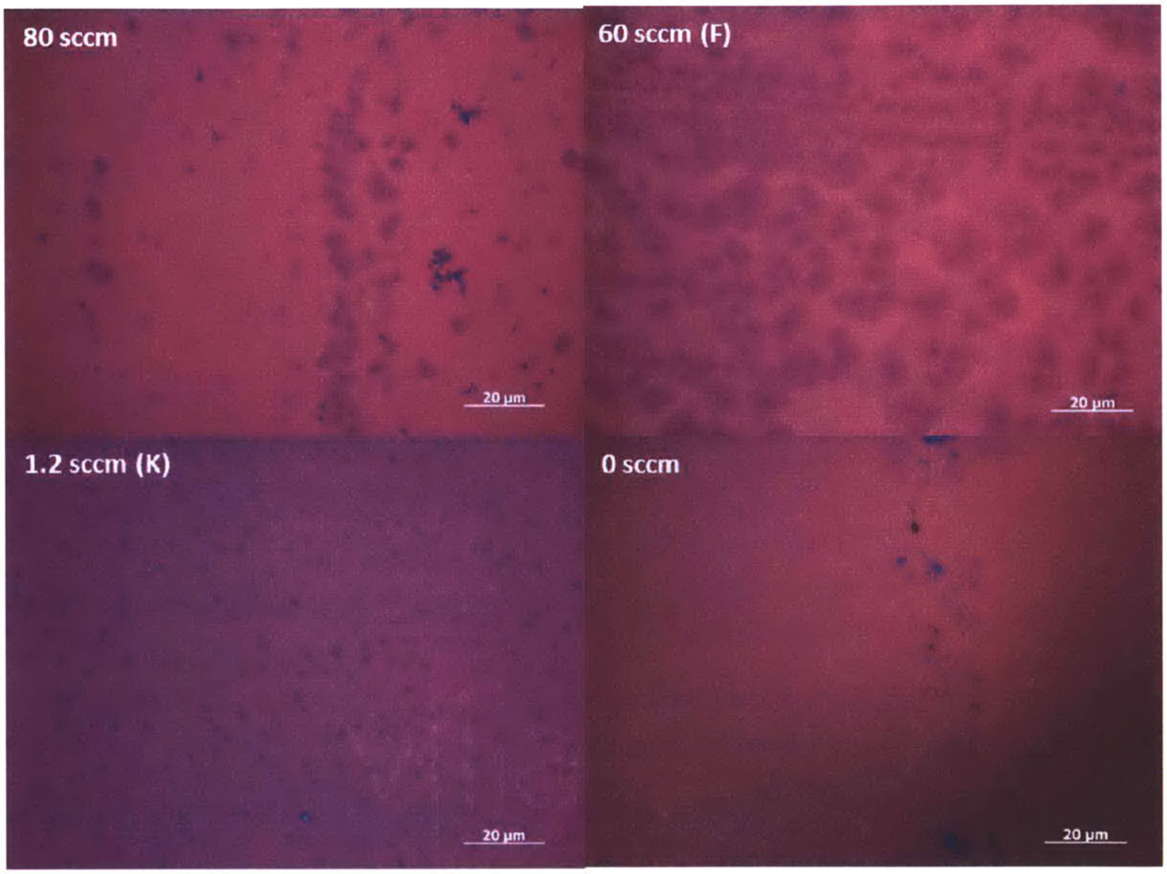

Figure 3.2. The optical microscope images of the graphene samples which are synthesized with the four extreme hydrogen flow rates

Fig. 3.2. shows the surface morphologies of four extreme hydrogen flow rate cases in the hydrogen controlled graphene synthesis. If the hydrogen is not introduced during the growth step, the synthesis of graphene does not occur as shown in the right bottom image of the Fig. 3.2. On

the other hand, if the hydrogen increases above the critical point ($H_2/Ar > 0.060$), the synthesized graphene becomes discontinuous.

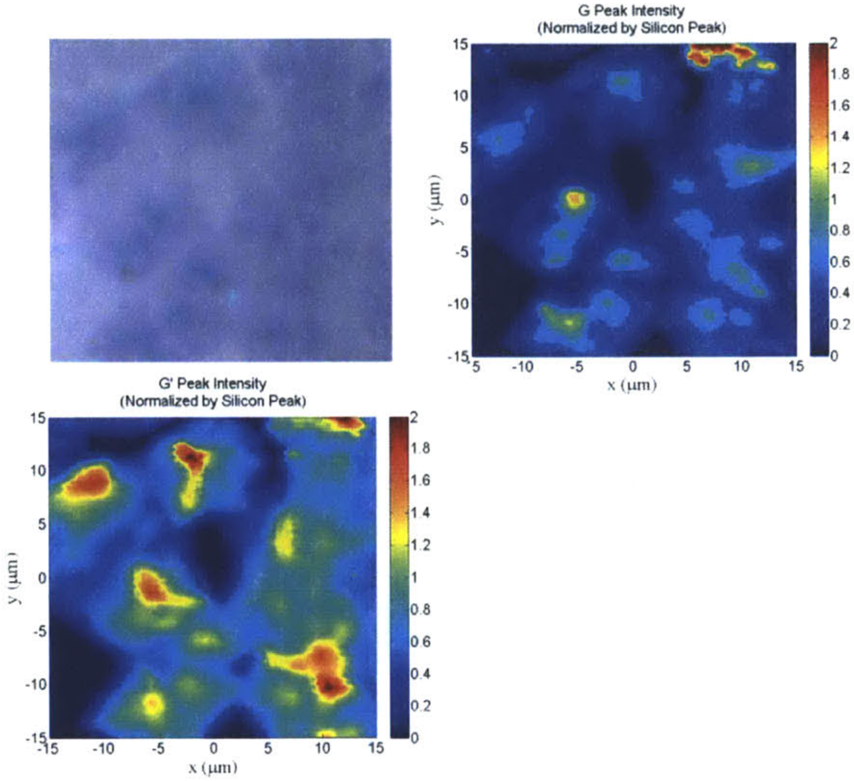

Figure 3.3. Raman mapping data and the optical microscope image of the graphene with lots of openings (H2/Ar = 0.060) Normalized G' and G peak shows the sharp contrast across the regions with and without graphene.

3.2. Sheet Resistance of Hydrogen Controlled Mono-to-Multilayer Graphene

The sheet resistance data with respect to the hydrogen flow rate is presented in the Fig. 3.4. Overall, the sheet resistance of hydrogen controlled single-to-multilayer graphene is low and stable for the wide window of hydrogen. In case of low to relatively high hydrogen flow rate region ($0.005 < H_2/Ar < 0.040$), the sheet resistance of synthesized graphene decreases as the hydrogen flow rate increases. However, the two extreme cases ($H_2/Ar = 0.0012$, $H_2/Ar = 0.060$) deviate from the global trend.

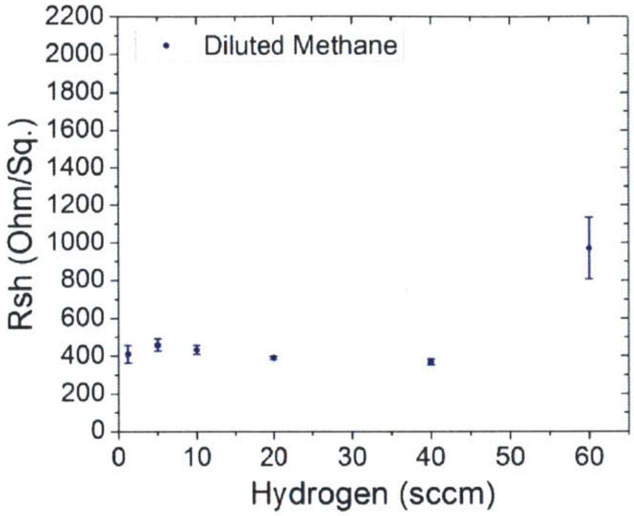

Figure 3.4. The sheet resistance data with respect to the hydrogen flow rate

3.3. Dependence of Transmittance on Hydrogen Flow Rate.

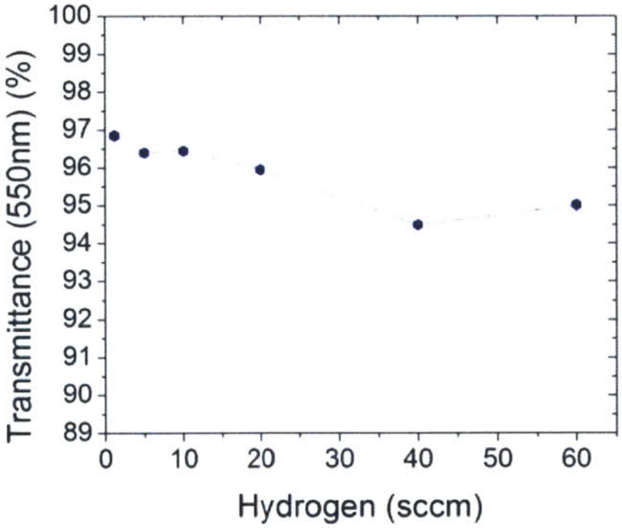

Figure 3.5. Transmittance vs. Hydrogen flow rate graph of the hydrogen controlled single-to-multilayer graphene

The transmittance data of the hydrogen controlled graphene samples reflect the surface morphologies. Consistent with the observation in the surface morphology section, the transmittance is improved as the hydrogen flow rate decreases. However, the sensitivity of transmittance with respect to the hydrogen flow rate is much lower than for methane flow rate. This is partially due to the low methane concentration of the diluted methane; the transmittance sensitivity with respect to the hydrogen flow rate could become larger if the methane flow rate increases.

3.4. Carrier Mobility

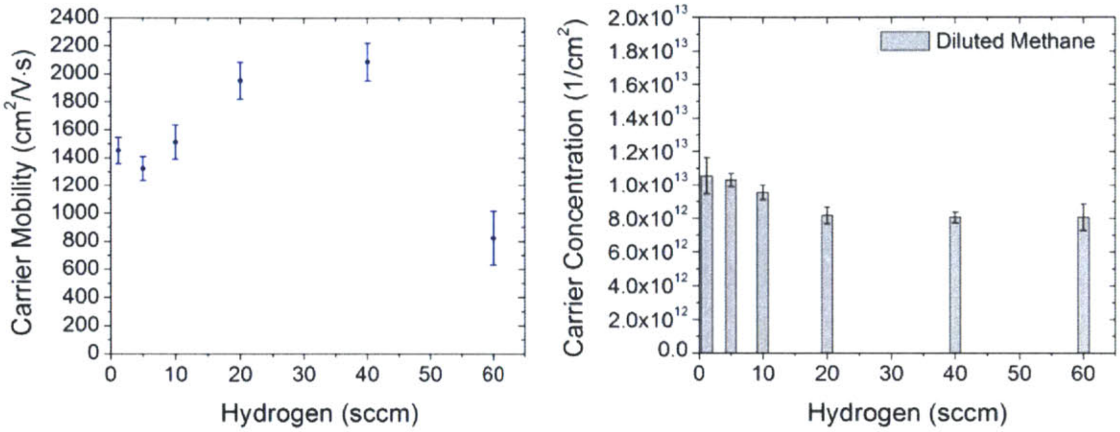

Figure 3.6. Carrier mobility and carrier concentration data with respect to the hydrogen flow rate

Carrier mobility of the hydrogen controlled graphene shows very different trends compare to the methane controlled graphene case. Except for two extreme hydrogen flow rate cases (H_2/Ar = 0.0012, H_2/Ar = 0.060), the carrier mobility increases as the hydrogen flow rate rises. Therefore, the carrier mobility has positive correlation with the hydrogen flow rate for the wide hydrogen window. The reasons why two carrier mobility values for the two extreme cases deviate from the global trend are explained in the discussion section.

3.5. Quality of Hydrogen Controlled Graphene

The DC to optical conductivity ratio is chosen as the parameter to evaluate the quality of graphene in the last chapter. Because the metric takes both transmittance and sheet resistance into account, the tendency becomes more complicated. Even though the sheet resistance increases when the hydrogen flow rate diminishes, the ratio becomes higher due to the increasing transmittance. Therefore, roughly, the ratio is negatively correlated with the hydrogen flow rate.

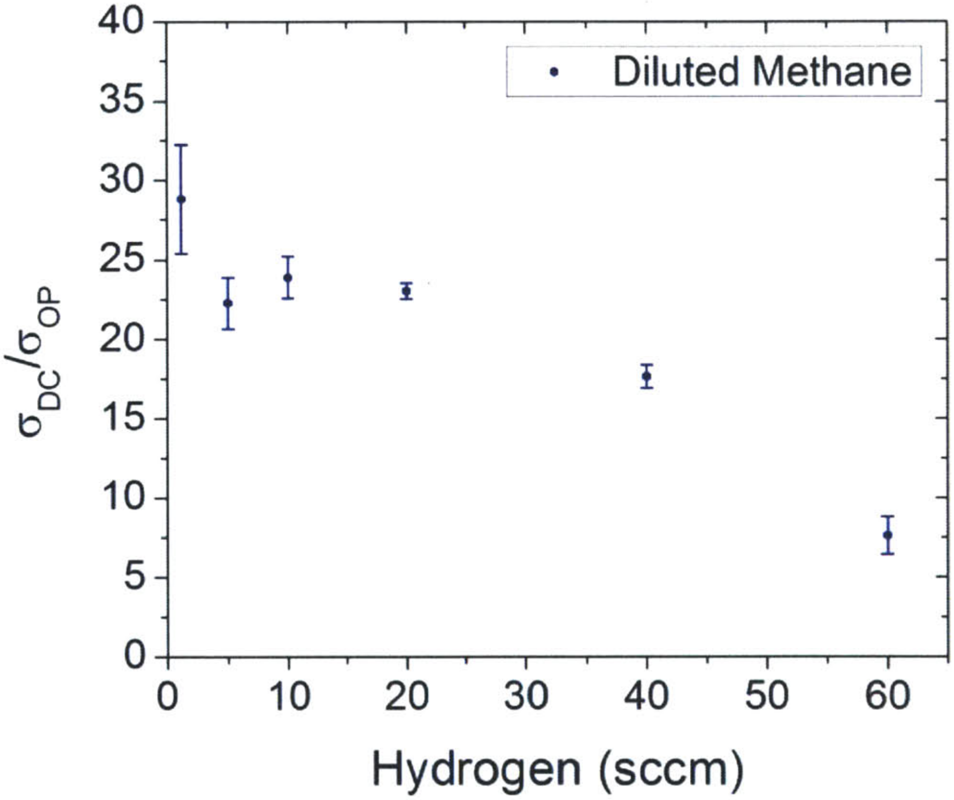

Figure 3.7. The DC to optical conductivity ratio of the hydrogen controlled single-to-multilayer grpahene

3.6. Raman Mapping

Fig. 3.8 and 3.9 are the images provide the defect distribution and the quality of the synthesized graphene. Interestingly the distributions of D/G ratio are similar for the hydrogen controlled single to multilayer graphene. In addition, the average D/G ratios of the scanned areas are very low. As the author mentioned above, this is related to the low methane concentration.

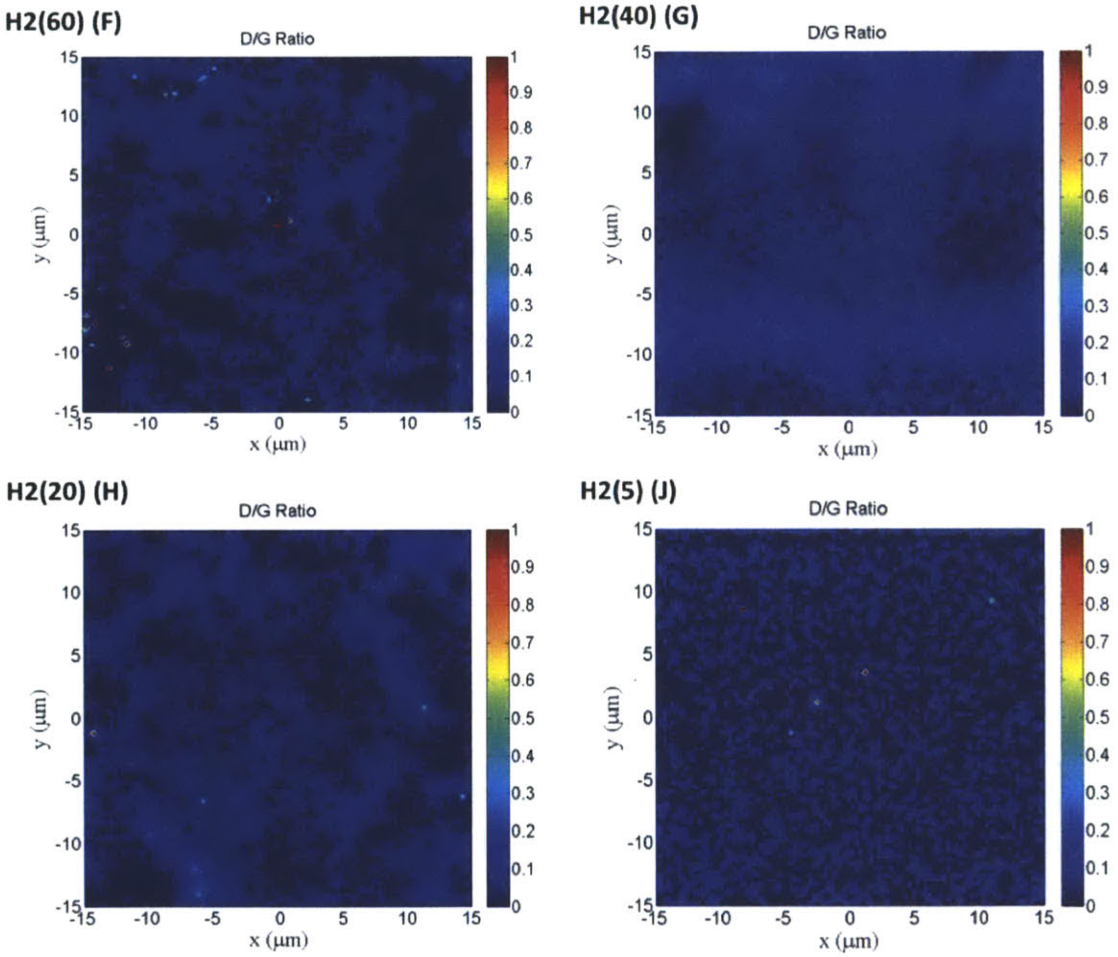

Figure 3.8. D/G ratio of the hydrogen controlled single-to-multilayer graphene

On the other hand, the distribution of G'/G ratio varies greatly with respect to hydrogen flow rate. The area of the high G'/G ratio region increases as the hydrogen flow rate decreases. This is consistent with images from the optical microscope. With the low D/G ratio and various G'/G ratio, the true meaning of multilayer synthesis is possible. As the hydrogen decrease to 5sccm (H2/Ar = 0.005), the G'/G ratio of the graphene varies in the range of 2.5 to 3 which is consistent with monolayer graphene.

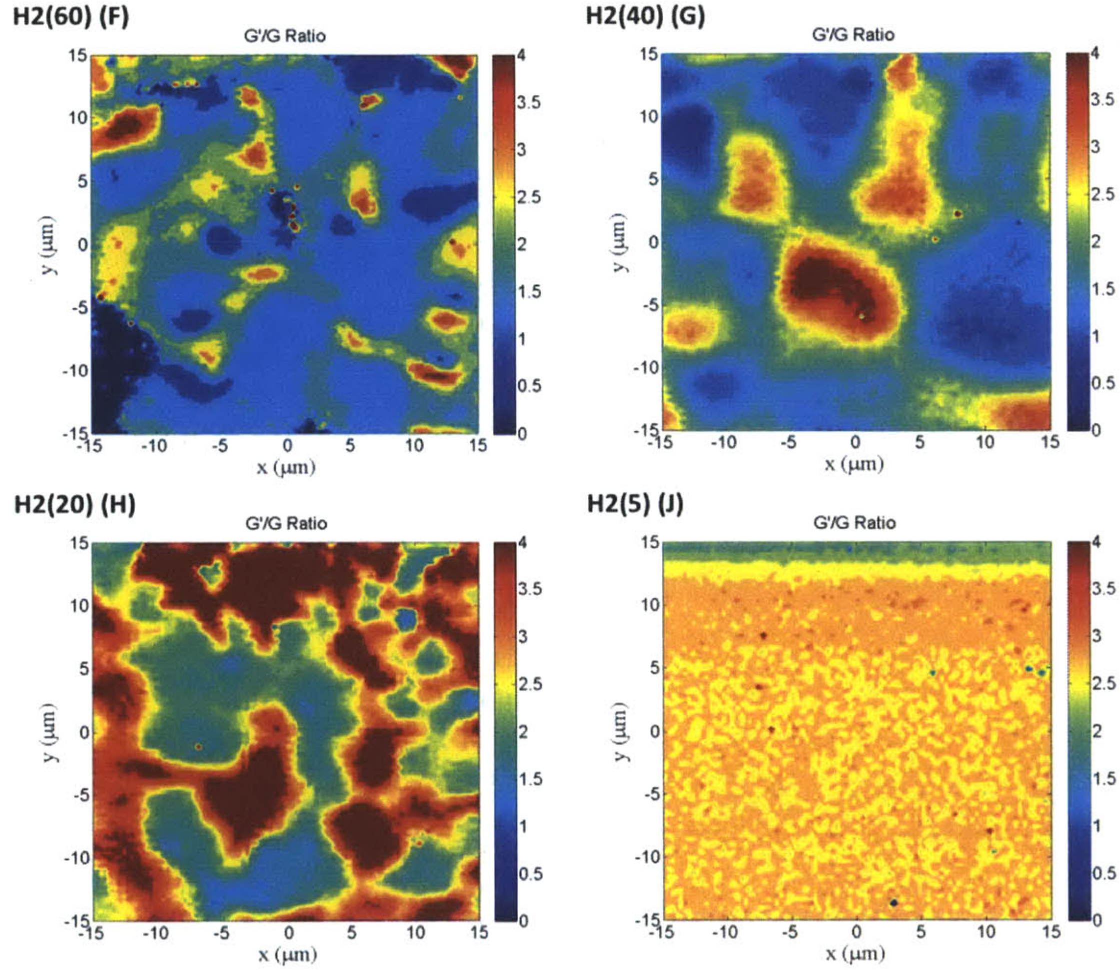

Figure 3.9. D/G ratio of the hydrogen controlled single-to-multilayer graphene

3.7. Discussion

(1) Surface morphologies and transmittance of hydrogen controlled APCVD graphene

In the continuous regime ($H_2/Ar < 0.04$ for 100ppm diluted methane), the number of layers decreases as the hydrogen flow rate diminishes. For higher hydrogen flow rate case ($H_2/Ar > 0.06$), the graphene is etched away by the large hydrogen flow. This is due to the two different effects of hydrogen, which are surface activator and etching reagent as Ivan Vlassiouk et al.[11] suggests. When the hydrogen flow rate is lower than a critical point ($H_2/Ar < 0.040$), the hydrogen aids the creation of active carbon species. Hydrogen molecules that are absorbed through the copper surface are decomposed to the active radical and react with carbon species. This process increases the concentration of active carbon species, and the larger number of active molecules results in thicker graphene. When the hydrogen flow rate is higher than critical point ($H_2/Ar > 0.060$), the monolayer background is etched away by the large hydrogen flow. F in Fig. 3.1 shows the graphene synthesized in high hydrogen flow conditions. The graphene has openings all around the area, and the author confirmed that the brighter areas are holes rather than monolayer background using Raman mapping. Fig. 3.3 is the optical microscope picture, and Raman mapping data collected in the same region. The intensity of G and G` peaks are normalized by the silicon peak. The intensity of G and G` peaks become zero at the brighter areas. Therefore, the brighter areas are openings, and the polygonal edges imply that the graphene was etched away.

The effect of hydrogen can be also confirmed by exploring the two different extreme cases. In Fig. 3.2, the optical microscope images of those two cases ($H_2/Ar > 0.08$ or $H_2/Ar = 0$) are displayed. When the hydrogen flow rate is too high ($H_2/Ar > 0.08$), graphene is etched away by the hydrogen. In the other extreme, there is not enough hydrogen to activate copper surface sufficiently to form a continuous graphene sheet.

The transmittance data are consistent with the surface morphologies of hydrogen controlled graphene. When the hydrogen flow rate is lower than 40 sccm, the transmittance of graphene is negatively related to the hydrogen flow rate but slightly rises for the hydrogen flow rates larger than 60 sccm. This is because the openings in graphene does not absorb any incident light, thus increasing the overall transmittance.

(2) Sheet resistance and carrier mobility

As the author discussed in the previous chapter, the sheet resistance depends on the carrier concentration, and mobility. Therefore, it is natural to discuss the important factors that determine the carrier mobility and then explain the sheet resistance data of hydrogen controlled graphene. Before starting the discussion about the carrier mobility, we need to examine the Raman mapping data. For a large range of hydrogen flow rates (H_2/Ar: 0.005 ~ 0.060), the D/G ratios of the synthesized graphene are similar and very low compare to those of the methane controlled multilayer graphene. Since the defect density is low, $\mu_{lattice}$ plays more important role rather than $\mu_{impurities}$ in the hydrogen controlled graphene case. In other words, domain size of graphene becomes the main factor that changes carrier mobility and sheet resistance over different hydrogen flow rates. This is because if the average domain size of the graphene is small, the domain boundary per unit area is large which leads to the frequent scattering, which lowers the $\mu_{lattice}$, and μ consequently.

Since the synthesized graphene completely covers the copper foil except for the very high hydrogen flow rate condition (H_2/Ar: 0.060, CH_4/H_2:0.00167), the nucleation density represents the average domain size of graphene. In other words, the lower nucleation density, the larger domain size of synthesized graphene. Wenhua Zhang et al.[15] claimed that the lower CH_4/H_2 ratio leads to the less nucleation density from their calculation results. This is because the chemical potential of C in equilibrium is lower when the CH4/H2 is higher. In addition, as we discussed in the last chapter, the hydrogen acts like a surface activator in the low hydrogen flow rate region. Refer to 3.6. When the hydrogen flow rate is in the 5 to 40 sccm range, carrier mobility of graphene rises as the hydrogen flow rate increases due to the decreasing nucleation density. However, the carrier mobility at the two extreme cases, K and F, deviates from this trend. In case of K, the hydrogen flow rate is very low (H_2/Ar: 0.0012, CH4/H2: 0.0833); thus the hydrogen cannot fully activate the copper surface which leads to lower nucleation density and larger domain size. On the other hand, F (H_2: 60sccm) shows lowest carrier mobility among the hydrogen controlled single-to-multilayer graphene. Since hydrogen etched away some parts of the graphene and created many openings, the measured mobility of F condition becomes exceptionally low.

From the Fig. 3.6, the author found that carrier mobilities of hydrogen controlled single-to-multilayer graphene have mobilities greater than $1300\,\mathrm{cm}^2/\mathrm{V}\cdot\mathrm{s}$ except the discontinuous graphene. This value is similar to the largest mobility measured from the methane controlled single-to-multilayer graphene. And the largest mobility of methane controlled graphene was achieved when the graphene has very low defect density similar to that of the hydrogen controlled graphene. From this observation, we estimate that $\mu_{lattice}$ has range equal to or larger than $1300\,\mathrm{cm}^2/\mathrm{V}\cdot\mathrm{s}$ with $1 \times 10^{13}\mathrm{cm}^2$ carrier concentration for APCVD graphene.

Now, let us examine the sheet resistance graph in Fig. 3.4. The sheet resistance data are consistent with the author's observations in the mobility data. The sheet resistance decreases as hydrogen flow rate increases except for extreme cases. Activation of copper surface and the etching reaction by the hydrogen create the deviations.

Compared to the mobility data, the sheet resistance shows less change when hydrogen flow rate is varied. This is because in addition to the mobility, carrier concentration also plays a role in the sheet resistance. Fig. 3.6 presents the carrier concentrations of the different growth conditions, and the author observed that the carrier concentration decreases as the number of layer increases. (Except two extreme cases, the number of layer increases as the hydrogen flow rate rises.) This is because the monolayer background protects the multilayer from the doping effects.

(3) Evaluation of hydrogen controlled single-to-multilayer graphene as a transparent electrode

Fig. 3.7 shows the DC-to-optical conductivity ratios of hydrogen controlled mono-to-multilayer graphene. Overall quality of hydrogen controlled graphene surpasses that of the methane controlled graphene. This is because the author kept the methane flow rate much lower (CH_4/Ar: 100ppm) than that of the methane controlled case, and hydrogen is not detrimental to the defect density of graphene. The DC-to-optical conductivity ratio diminishes as hydrogen flow rate rises because of the decreasing transmittance. However, in practice, robust graphene with lower sheet resistance and intermediate transmittance could be better for the transparent electrodes. Therefore, both thin and thick graphene films should be considered and tested for future applications.

From the hydrogen controlled single-to-multilayer graphene study, the author synthesized mono to multilayer graphene by varying the hydrogen flow rate. Except the extreme cases ($CH_4/H_2 > 0.0833$ or $CH_4/H_2 < 0.00167$), the sheet resistance and mobility are improved when the hydrogen flow rate increases. This is due to the lower nucleation density and larger domain size that lead to the higher μ_{lattice}. In addition, the number of graphene layers rises when the more hydrogen flow is supplied through the chamber. This is because the more hydrogen flow rate creates more active carbon species which results in the thicker graphene.

The hydrogen controlled graphene will be very useful because of its great electrical and optical properties. Also, the control of number of layers is readily achievable with this approach. High DC-to-optical conductivity ratio up to 28.8 is achieved in this study, and further improvement through temperature control is presented in the next chapter.

Chapter 4. Growth Temperature Study

Throughout the previous two chapters, two major growth parameters for the single-to-multilayer graphene synthesis were studied. In this chapter, the temperature during annealing and the growth steps becomes the independent variable to enhance the quality and suppress the multilayer islands of the synthesized graphene. Since increasing temperature increases the desorption rate of the carbon species, higher quality single layer graphene is expected at higher temperature. The temperature study was conducted with the single layer graphene presented in chapter 3. As summarized in the table 4.1, the graphene samples were synthesized at 1000, 1035, and 1070°C. (Normal growth temperature: 1000°C, The melting point of the copper: 1084.5°C). The surface morphology and electrical/optical characteristics of the temperature-tuned graphene are shown in subsequent sections.

Condition Temp. (°C)	$H_2(5)Ar - a(1000)$
1000	L
1035	M
1070	N

Table 4.1. The various growth temperatures for the high quality single layer graphene synthesis

4.1. Surface Morphologies

Figure 4.1. Optical microscope images of the graphene synthesized at different temperatures

Fig. 4.1 is shows the effect of growth temperature on the morphology of synthesized graphene. Basically, the diluted methane with the low hydrogen flow rate (H2/Ar = 0.005) leads to the formation of single layer graphene with bilayer islands. As the growth temperature increases, the density of bilayer island decreases and very clean single layer graphene is achieved at 1070°C.

4.2. Sheet Resistance with respect to Growth Temperature

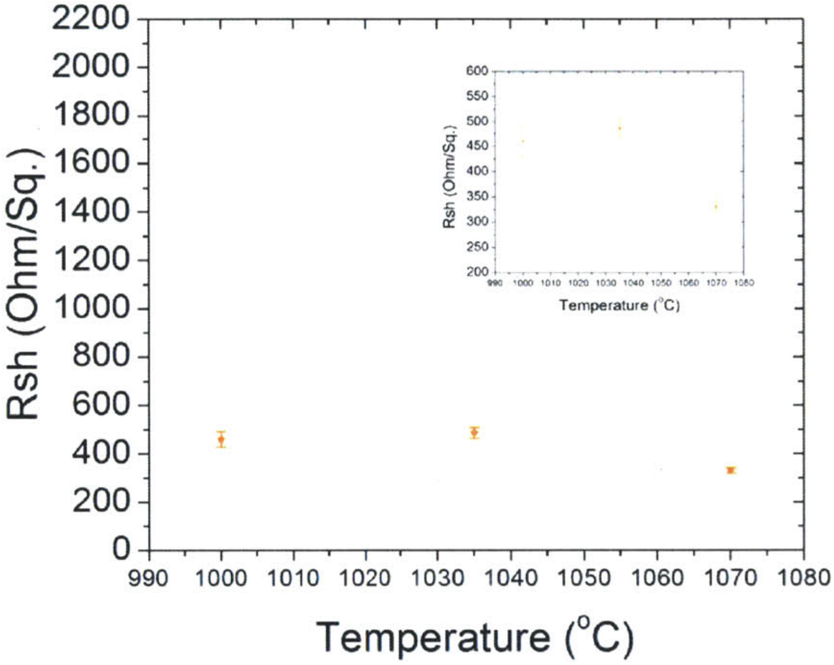

Figure 4.2. Sheet resistance data of the growth temperature tuned graphene

The sheet resistance of the growth temperature tuned graphene is presented in the Fig. 4.2. As temperature increases the sheet resistance increases slightly and then decreases to the lowest sheet resistance among all conditions presented in this thesis. Since the average sheet resistance of the graphene synthesized at 1035°C falls down to the standard deviation range of the graphene grown at 1000°C, the difference in the sheet resistance data of those two condition is not statistically meaningful. Therefore, the change in growth temperature up to 1035°C does not present significant difference in sheet resistance. On the other hand, the sheet resistance of graphene synthesized at 1070°C shows 28% improvement from that of the graphene grown at 1000°C. The average sheet resistance of the graphene synthesized at 1070°C is 331(Ω/□). Also, the mobility is 2039 ($cm^2/V \cdot s$), which is the highest value among all conditions in this work. Therefore, the sheet resistance can be further improved by doping to the saturation point of the mobility.

4.3. Transmittance

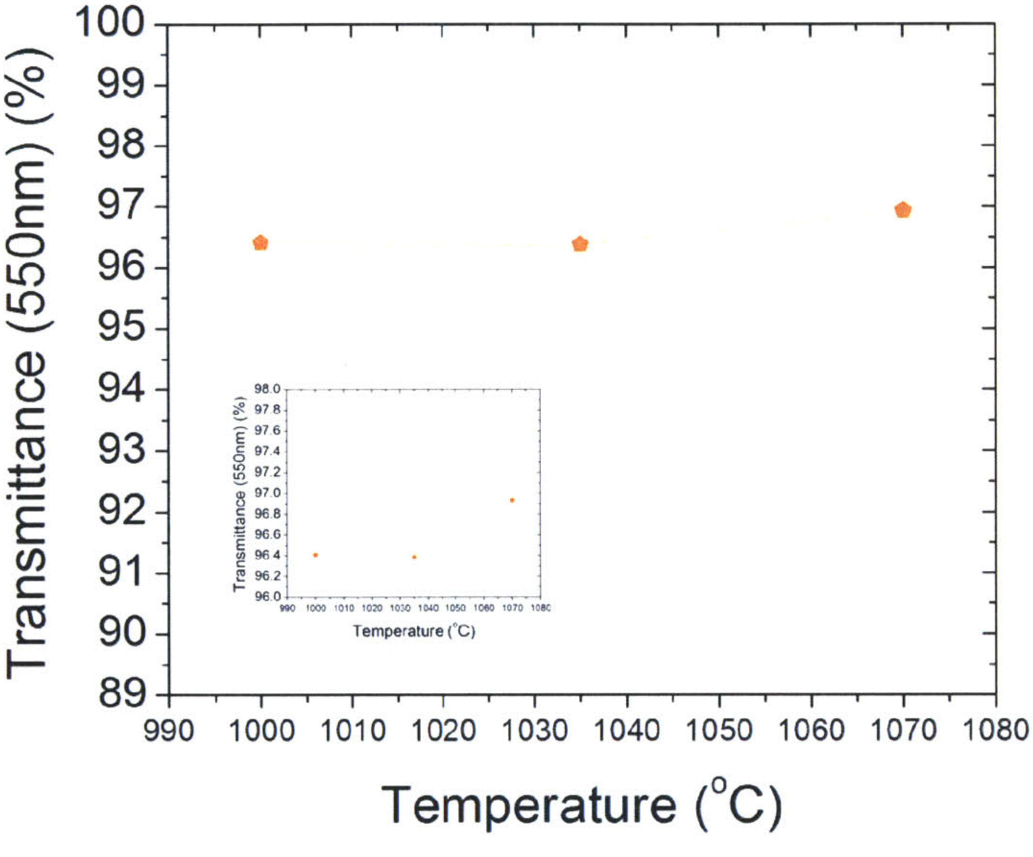

Figure 4.3. Transmittance data vs. Growth temperature

The transmittance data of growth temperature tuned graphene confirms the author's observation in the surface morphology section. The transmittance of the synthesized graphene increases as temperature rises (after 1035°C point) due to the decreasing bilayer area. Because this flow rate condition already creates single-layer graphene with few bilayer islands at 1000°C, the effect of growth temperature on the transmittance is not dramatic. Further study with thicker graphene condition will show clearer tendency with respect to the growth temperature.

4.4. Carrier Mobility

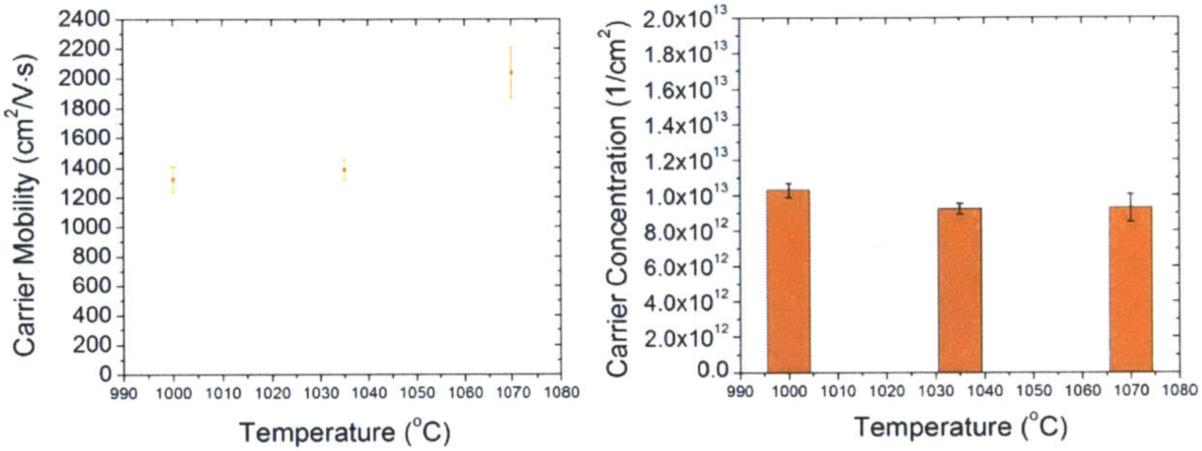

Figure 4.4 Carrier mobility and carrier concentration data of the growth temperature tuned graphene

According to the carrier mobility data shown in the Fig. 4.4, the growth temperature optimization process enhances the carrier mobility of synthesized graphene. Carrier mobility shows positive correlation with the growth temperature, and the average mobility up to 2039 ($cm^2/V \cdot s$) is achieved at 1070°C. Further improvement of graphene quality may be possible by increasing the growth temperature up to melting point of the copper. Also, graphene synthesis on melted copper is another way to enhance the quality.[19][20]

4.5. Quality of Graphene as a Transparent Conductive Film

The DC to optical conductivity ratio shows a large improvement when the growth temperature increases. Since the higher growth temperature suppresses the formation of bilayers, and decreases the sheet resistance, the DC to optical conductivity ratio increase by a large amount. The average ratio reaches 36.3 at 1070°C which is a 62.8% improvement from the original value at 1000°C. The effect of temperature is dramatic and the further study with other conditions may be worth pursuing.

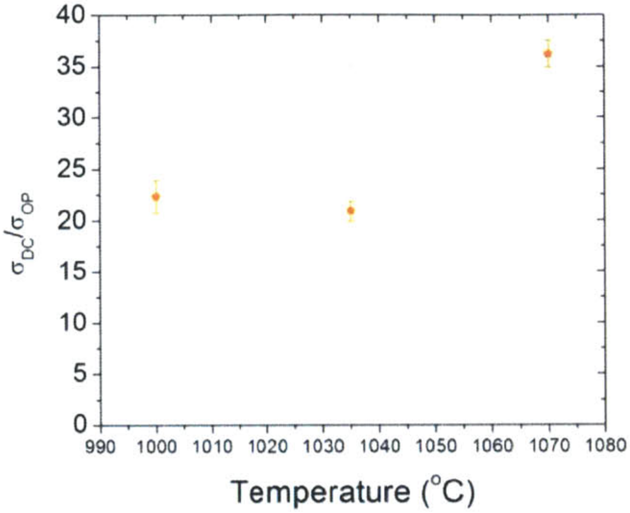

Figure 4.5. The DC to optical conductivity ratio vs. Growth temperature

4.6. Raman Mapping

Fig. 4.6 is the D/G ratio data extracted from Raman mapping results. The defect density becomes lower as temperature increases (T > 1035°C), and uniform over the area. The Fig. 4.7 is G'/G ratio maps over the scanned areas. The variation of G'/G ratio in the graphene synthesized at 1035°C is larger than other two conditions, and it is yet to be understood. Other than that, the G'/G maps of three different conditions confirms the presence single layer graphene.

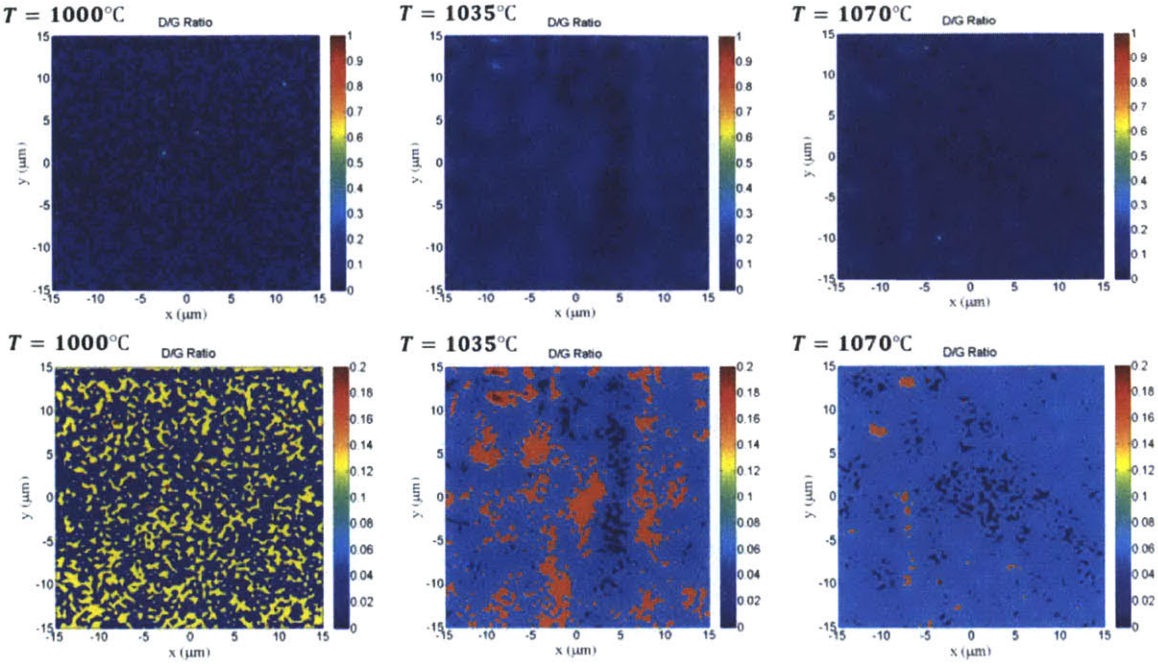

Figure 4.6. The D/G ratio of growth temperature tuned graphene at low contrast (Top), and at high contrast (Bottom)

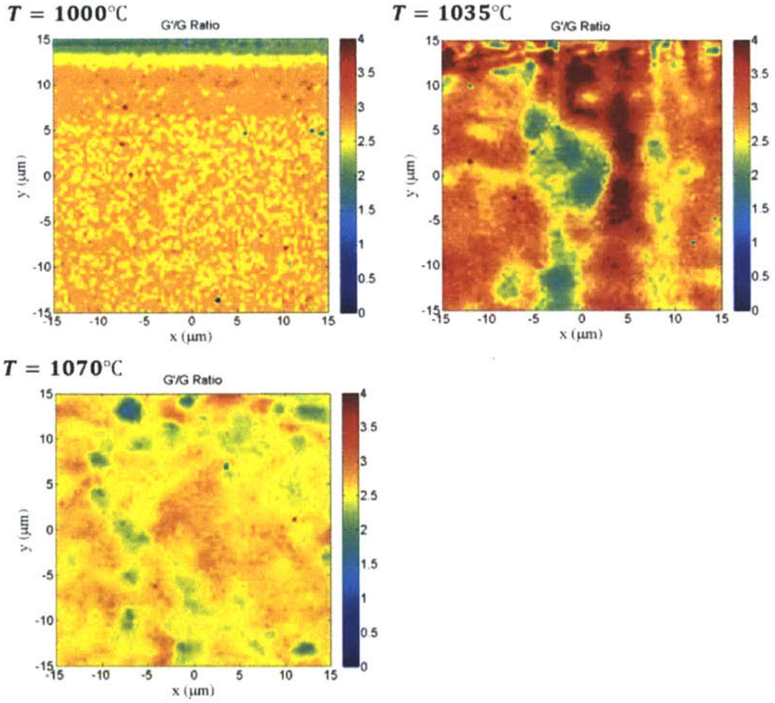

Figure 4.7. G'/G ratio of growth temperature tuned graphene

4.7. Discussion

(1) Surface morphologies and transmittance

In the hydrogen controlled mono-to-multilayer graphene, the synthesized graphene has some bilayer islands even with very low hydrogen flow rate (H_2/Ar: 0.0012). The clean monolayer graphene could be achieved by using higher growth temperatures. Since desorption rate of carbon species increases as growth temperature rises, the synthesized graphene has lower bilayer island density in case of high growth temperature. This tendency is observed both in optical microscope images (Fig. 4.1), and transmittance data (Fig. 4.3). The bilayer density decreases as temperature increases from 1000°C to 1070°C (melting temperature of copper: 1084.5°C) in Fig. 4.1 and the transmittance rises to 96.9% which is close to that of monolayer graphene.).

(2) Sheet resistance and mobility

The mobility of graphene increases dramatically when the temperature rises as shown in the Fig. 4.4. At 1070°C the mobility of graphene rises to 2039 ($\mathrm{cm^2/V \cdot s}$) which is a 54.1% improvement over the mobility at 1000°C. Once again, from Matthiessen's, rule which is shown below, the total mobility can be decomposed into different factors. From Raman mapping data (Fig. 4.6) the author found that there is slight change in defect density. As temperature rises, the defect density becomes slightly lower and uniform over the entire area.

$$\frac{1}{\mu} = \frac{1}{\mu_{impurities}} + \frac{1}{\mu_{lattice}} + \frac{1}{\mu_{defects}} + \cdots$$

The decrease in defect density has very little impact on increasing total mobility. However, the domain size is more important factor in this case because the variation of defect density over the different conditions is very small. As growth temperature increases, the desorption rate of carbon species becomes larger which results in lower nucleation density and larger domain size. Therefore, the synthesized graphene shows larger mobility and lower sheet resistance at the high growth temperature condition.

(3) Evaluation of temperature tuned graphene as a transparent electrode

As we discussed in previous chapters, the DC-to-optical conductivity ratio is positively related to the transmittance and negatively related to the sheet resistance. Thus, the ratio is improved as the growth temperature increases. When the growth temperature reaches 1070°C, the DC-to-optical conductivity ratio becomes 36.26 which is highest value among all the conditions discussed. This value is three times larger than the values Sukanta De et al.[14] calculated ($\sigma_{DC}/\sigma_{OP} = 11$) for the CVD graphene and above 35 which is the threshold value for the industrial application suggested by Sukanta De et al.[14] This proves that very high quality graphene can be synthesized by APCVD. The author expects that further improving quality is possible by tuning the hydrogen flow rate at high temperatures.

From the growth temperature study of APCVD graphene, the author found that the improvement of sheet resistance, mobility, and transmittance takes place at the high growth temperature. Attribute to the larger desorption rate of carbon species at higher temperature, both nucleation and bilayer growth are suppressed. Therefore, the synthesized graphene has larger average domain size and lower bilayer islands density. Finally, the larger domain size reduces the scattering rate which leads to high carrier mobility and lower sheet resistance. Further improving graphene quality may be achieved by the tuning of hydrogen flow rate.

The controls of the graphene synthesis with two major gases and growth temperature have been studied. After this chapter, the author examines the effect of annealing step on graphene synthesis.

Chapter 5. Annealing Step Study

The growth controls by methane and hydrogen gases are presented in chapter 2 and 3. And the effect of growth temperature tuning was studied in the last chapter. In this chapter, parameters in the annealing step will be used as independent variables. Specifically, the types of gases that flow during the annealing step are changed from conditions to conditions. Table 5.1 and 5.2 shows the two different annealing methods which are argon annealing and diluted hydrogen annealing (hydrogen is diluted by the argon gas during annealing step). In the tables, the gas flow rates over the CVD process are summarized for each different annealing method. Two tables are differing in "Ramp", and "Annealing" steps. Table 5.1 represents the argon annealing method and table 5.2 shows the diluted hydrogen method. In case of argon annealing method, 1000sccm of argon is supplied during ramp and annealing step. On the other hand, in the diluted hydrogen annealing method, 160sccm of hydrogen and 1000sccm of argon gases are introduced. Combined with the hydrogen annealing methods in chapter 2, the three different annealing methods will be studied. Also, the methane flow rate (x) during the growth step is varied from 5 sccm to 0.4 sccm for each different annealing method. The conditions are organized in table 5.3, with respect to the annealing methods and the methane flow rate (x) during the growth step. This study sheds light on the influence of annealing methods over methane controlled single-to-multilayer synthesis.

Gas	**I**	**II**	**III**	**IV**
H_2(sccm)	**0**	**0**	**5**	**5**
CH_4(sccm)	**0**	**0**	**x**	**x**
Ar(sccm)	**1000**	**1000**	**1000**	**1000**

Table 5.1. The gas flow rates of each gas throughout the CVD process (Ar annealing)

Gas	**I**	**II**	**III**	**IV**
H_2(sccm)	**160**	**160**	**5**	**5**
CH_4(sccm)	**0**	**0**	x	x
Ar(sccm)	**1000**	**1000**	**1000**	**1000**

Table 5.2. The gas flow rates of each gas throughout the CVD process (Ar+H_2 annealing)

Annealing Step CH_4(x)	**H2(160)**	**Ar(1000)**	**H2(160)Ar(1000)**
5	A3	A4	A5
3.5	B3	B4	B5
2	C3	C4	C5
1	D3	D4	D5
0.4	E3	E4	E5

Table 5.3. The conditions sorted by annealing step and methane flow rates in the growth step

5.1. Surface Morphologies

The surface morphologies of argon annealed copper grown graphene are shown in Fig. 5.1. The morphologies of these graphene samples have three distinctive characteristics compare to the other two annealing methods. Firstly, the multilayer density of the graphene sheet is much lower than that of graphene with other annealing methods. Secondly, the multilayer regions are distributed non-uniformly. The synthesized graphene has many circular single layer areas surrounded by the dotted multilayer region. (This is observed by optical microscope with the low magnification lens) Lastly, the dotted shape on the single layer background is distributed over the entire surface. These characteristics are related to the inert property of argon gas.

Figure 5.1. Optical microscope images of argon annealed copper grown graphene samples

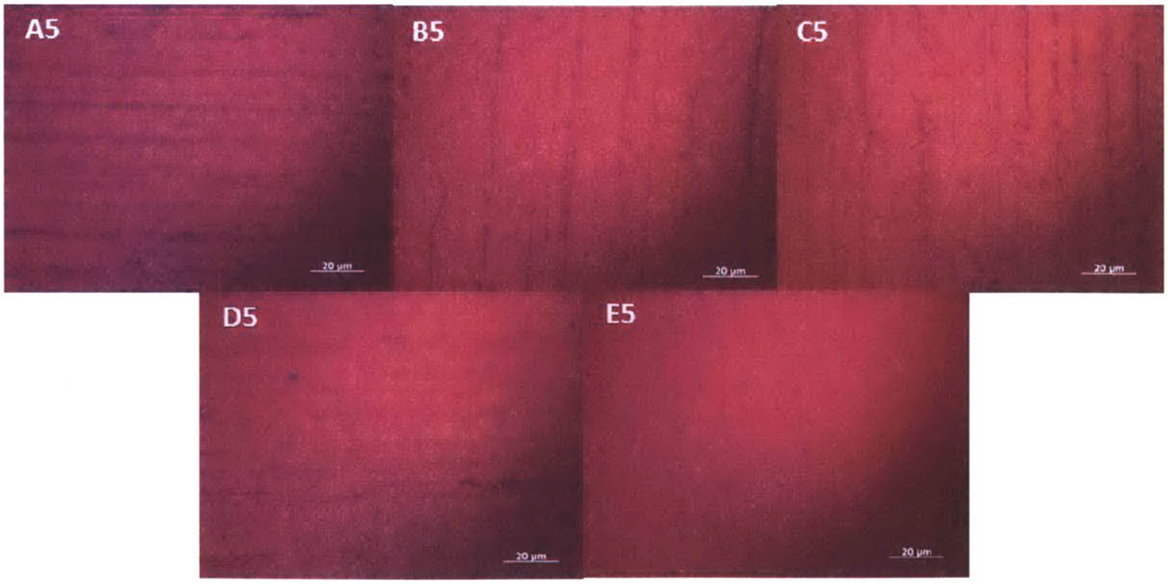

Figure 5.2. Optical microscope images of diluted hydrogen annealed copper grown graphene samples

On the other hand, the diluted hydrogen annealed copper grown graphene samples shows very similar surface morphology to the graphene with hydrogen annealing methods. The rolling line of the copper is highlighted by thicker graphene regions and many multilayer regions are distributed over the surface with more regular edge shapes. The only difference occurs when the methane flow rate is high ($CH_4/Ar = 0.005$). For this condition, the graphene with diluted hydrogen methods shows less, more regularly shaped multilayer regions.

5.2. Sheet Resistance of Annealing Step Tuned Graphene

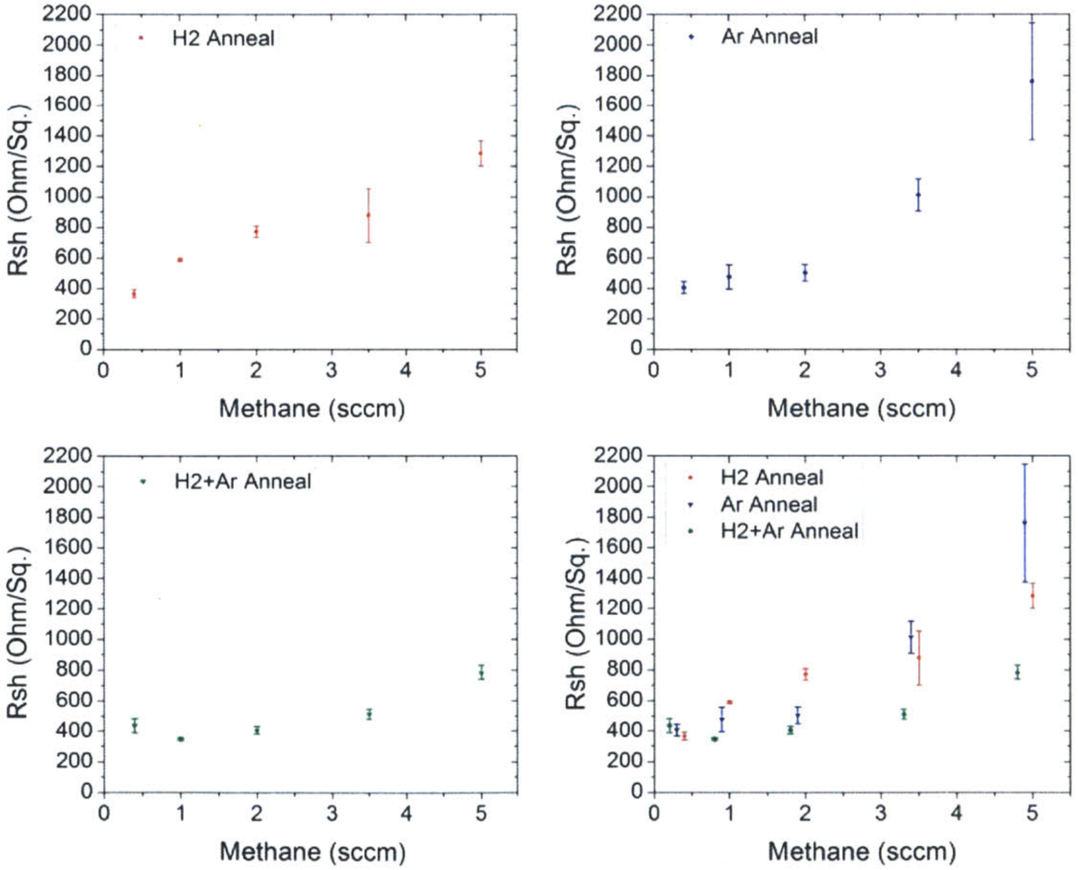

Figure 5.3. The sheet resistance data of the graphene samples with three different annealing methods

The sheet resistance data of the graphene from three different annealing methods are presented in the Fig. 5.3. Interestingly the sheet resistance of the graphene with diluted hydrogen annealing is low and less sensitive to the methane flow rate. For the methane flow rates higher than 1sccm ($CH_4/Ar > 0.001$), the graphene has 240~500 (Ω/□) lower sheet resistance than that of hydrogen annealing. On the other hand, the sheet resistance of the argon annealed copper grown graphene is insensitive to the methane flow rate when the growth condition is in the low methane flow rate region ($CH_4/Ar < 0.002$) but becomes more sensitive to the methane flow when the methane flow rate is high ($CH_4/Ar > 0.002$).

5.3. Transmittance

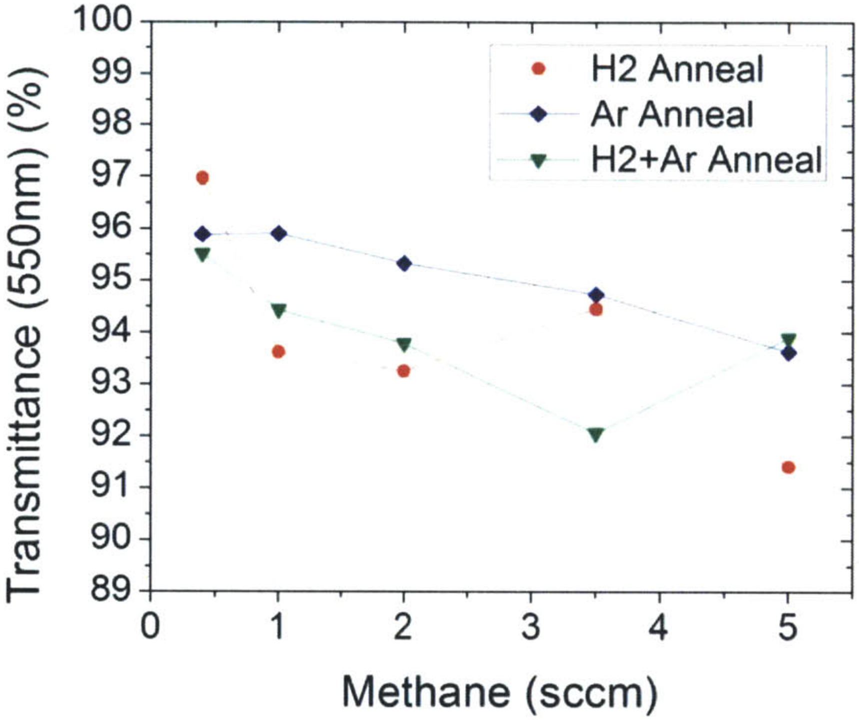

Figure 5.4. The transmittance data of graphene samples from three different annealing methods

The transmittance data of three different annealing methods provide more quantitative information about the morphology of the synthesized graphene. This is because the transmittance is related to the average number of graphene layers over the sample. In the Fig. 5.4, the graphene with argon annealing method has the largest transmittance among three different annealing methods with respect to the methane flow rate. The graphene with diluted methane method has larger transmittance than that of graphene from hydrogen annealing methods at three data points. At other two data points, the graphene with hydrogen annealing method shows the higher transmittance. Therefore it is hard to conclude which method has better transmittance between the diluted hydrogen annealing and hydrogen annealing methods.

5.4. Carrier Mobility

Fig. 5.5~5.8 are the carrier mobility and carrier concentration data for graphene samples from three different annealing methods. In the Fig. 5.8, the graphene from the diluted hydrogen annealing method shows superior carrier mobility data over those of graphene samples from other annealing methods. The carrier mobility of the diluted hydrogen method is roughly twice as high as that of other annealing methods. However, as the methane flow rate approaches 0.4 sccm ($CH_4/Ar = 0.0004$) the carrier mobility of those three different growth methods eventually merge together. The carrier mobility data from argon annealing and hydrogen annealing methods are very close for most conditions.

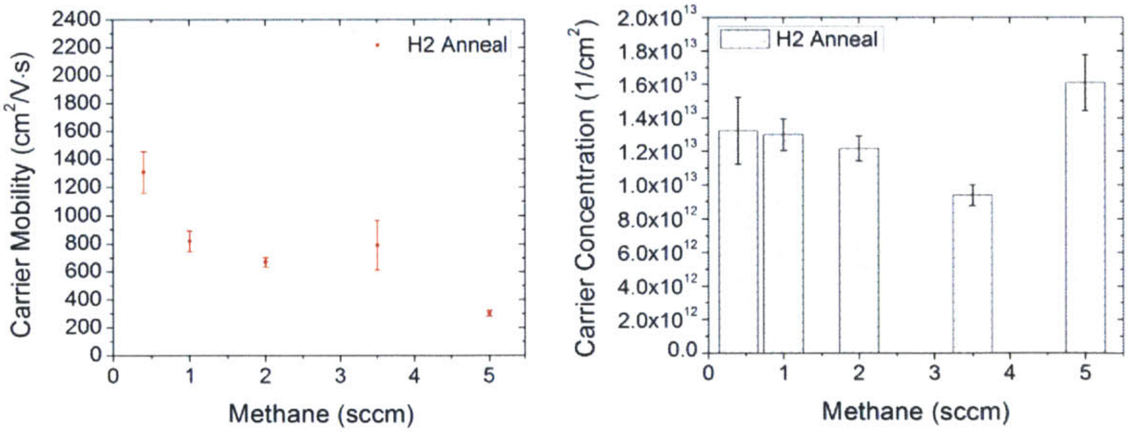

Figure 5.5. Carrier mobility and carrier concentration graphs of the graphene with hydrogen annealing methods

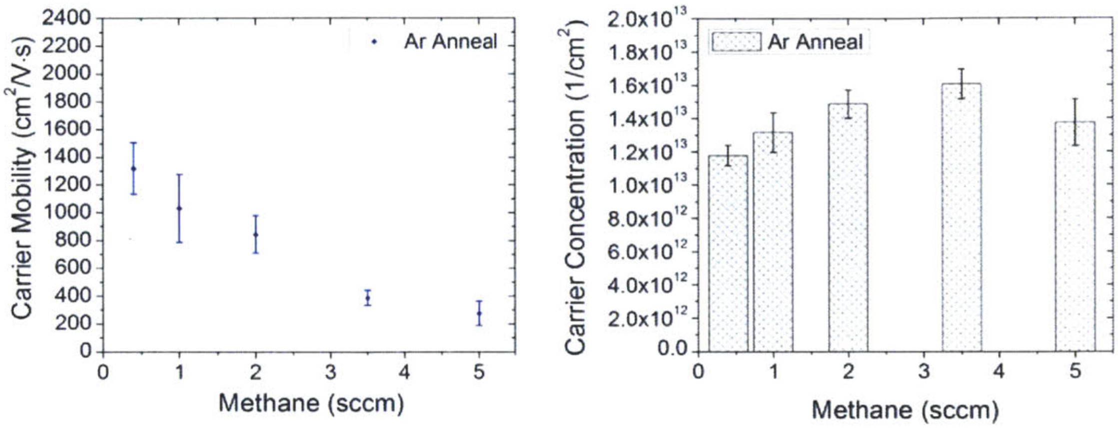

Figure 5.6. Carrier mobility and carrier concentration graphs of the graphene with argon annealing methods

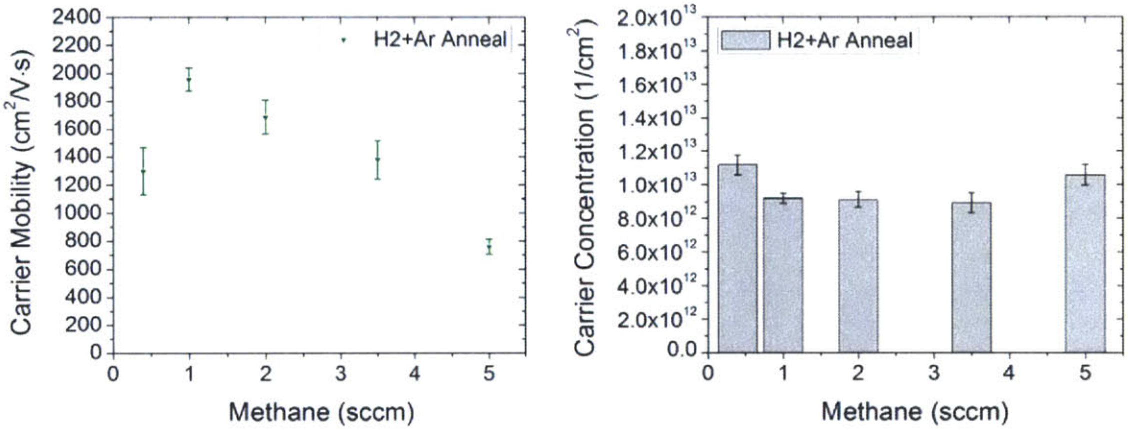

Figure 5.7. Carrier mobility and carrier concentration graphs of the graphene with diluted hydrogen annealing methods

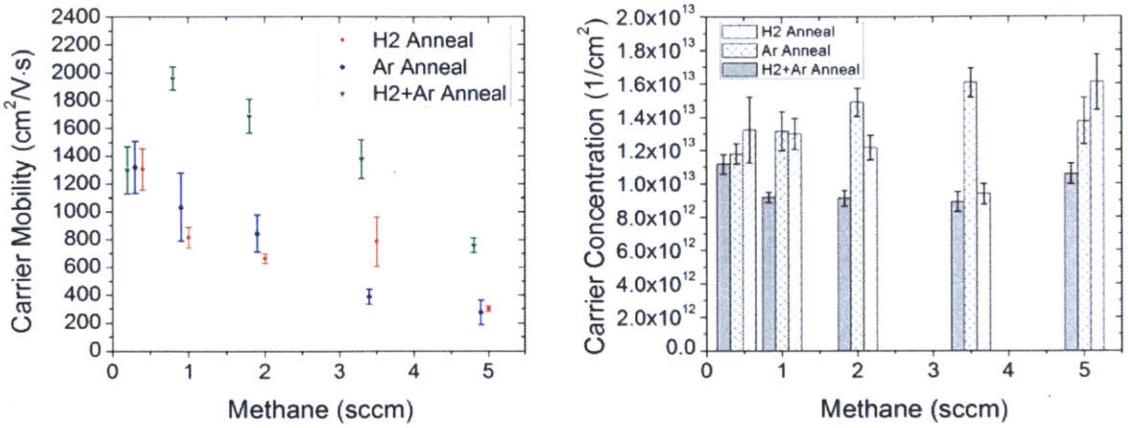

Figure 5.8. Carrier mobility and carrier concentration graphs of the graphene with three different annealing methods

5.5. Evaluating Graphene Quality

The DC to optical conductivity ratio is shown in Fig. 5.9. The ratio has negative correlation with the methane flow rate, similar to the results in the methane controlled single-to-multilayer graphene case. For a large range of methane flow ($0.0004 < CH4/Ar < 0.0035$), the ratio of graphene from diluted hydrogen annealing methods is similar to that of the graphene from argon annealing methods. Even though the sheet resistance of diluted hydrogen annealing methods is lower than that of the argon annealing method, the better transmittance of the argon annealing method compensates for the gap in sheet resistance. The DC to optical conductivity of the hydrogen annealing method is smaller than that of the other two methods for most methane flow rates. However, it eventually peaks at 0.4 sccm methane flow rate, due to the increases transmittance at that point.

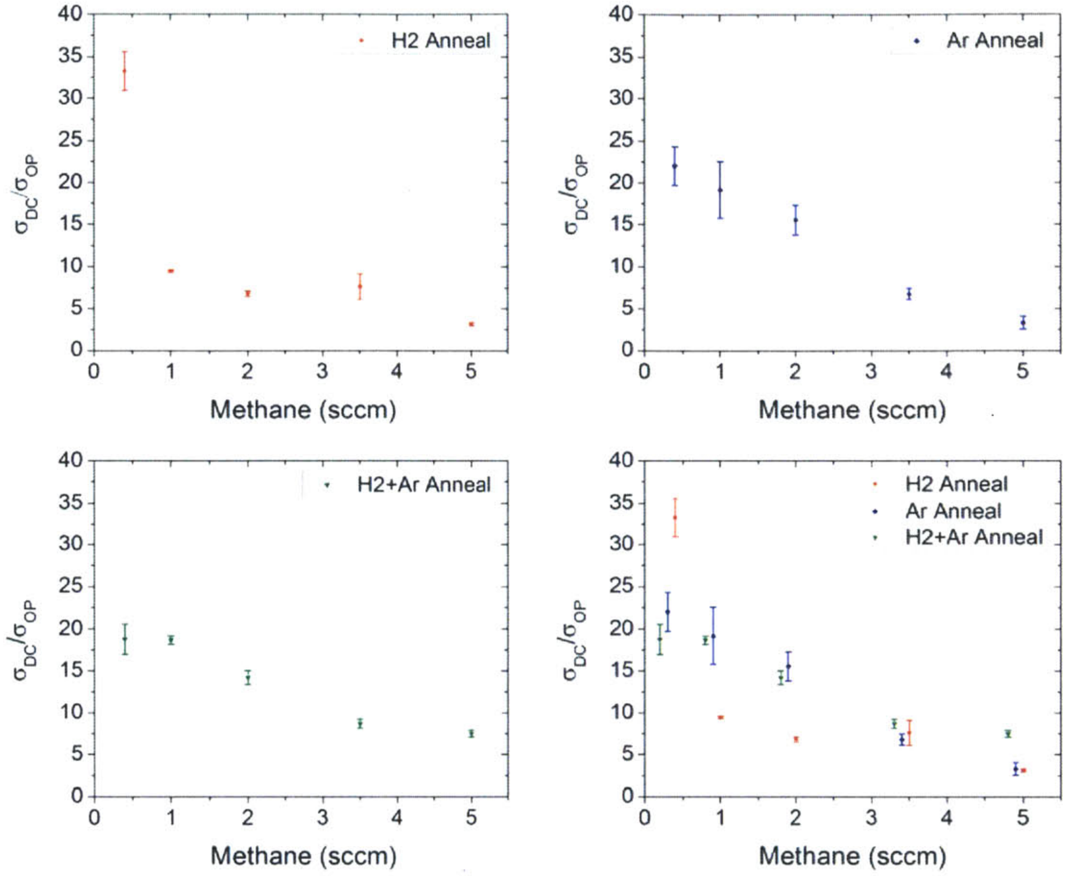

Figure 5.9. The DC to optical conductivity ratio data of three different annealing methods

5.6. Raman Mapping

Fig. 5.10 shows the D/G ratio data of the three different annealing methods synthesized with the high methane flow rate condition ($CH_4/Ar = 0.005$) during the growth step. The high methane flow rate condition is chosen in order to investigate why the diluted hydrogen annealing method has low sheet resistance even at high methane flow rate. The graphene from diluted hydrogen annealing method shows the low D/G ratio background with some highly defective regions. Hydrogen annealed copper grown graphene has similar high-defect islands, but more background defects. Lastly, the graphene from argon annealing method shows huge defect areas with more background defects compare to other two methods.

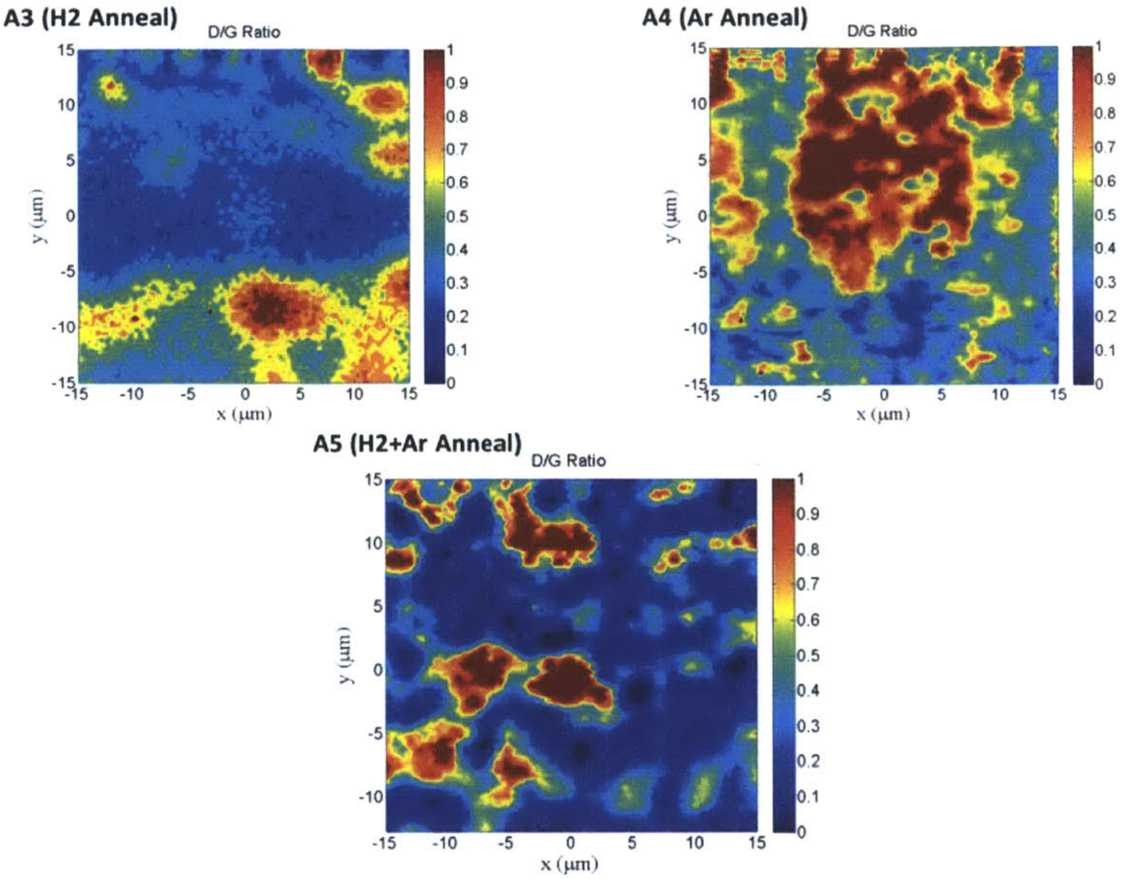

Figure 5.10. The D/G ratio maps of three different annealing methods

In addition to the D/G ratio data, G'/G ratio maps provide the qualitative information about the synthesized graphene. In this case, these data are useful for comparing the graphene samples from the diluted hydrogen and argon annealing methods. Even though the transmittance data of two graphene samples are almost identical, the G'/G data of those samples are completely different. Graphene from diluted hydrogen methods exhibits large monolayer regions. On the other hand, argon annealing method creates graphene with large defective amorphous carbon regions. (Large D/G ratio and small G'/G ratio)

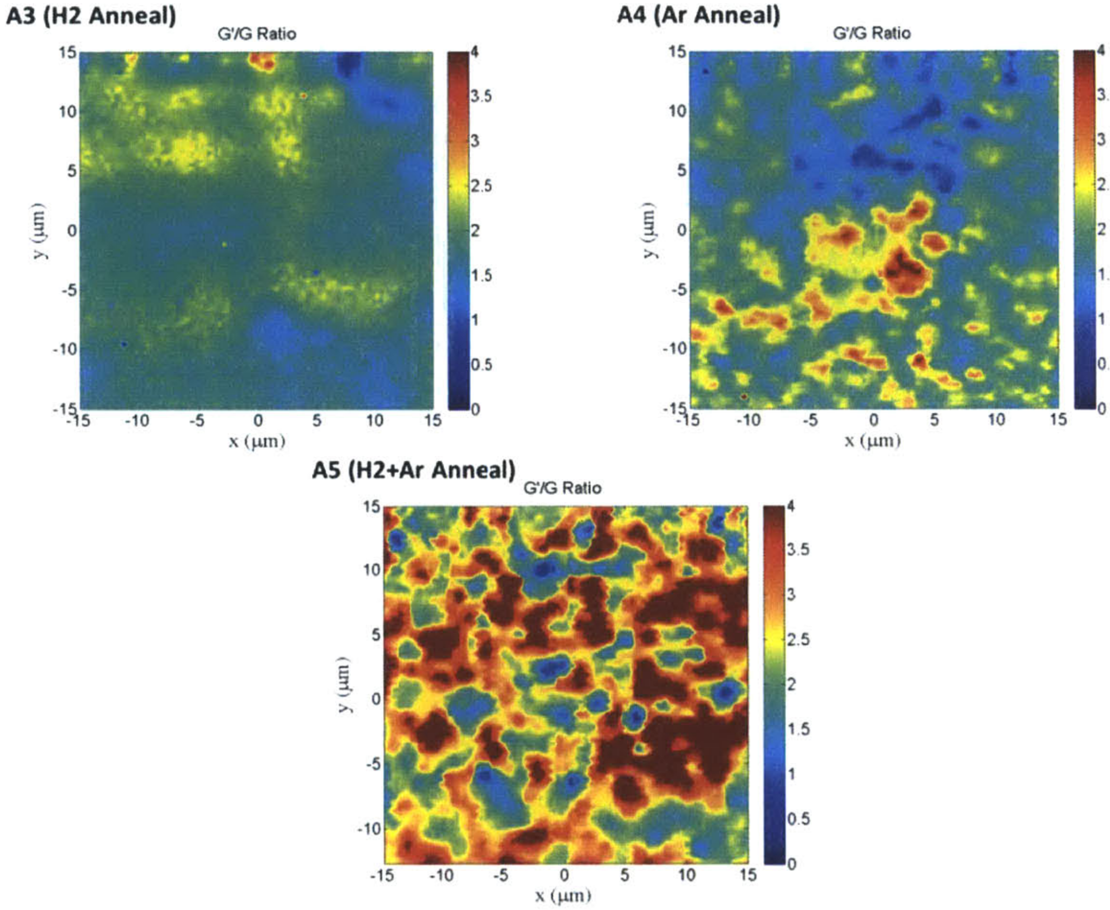

Figure 5.11. G'/G ratio maps of three different annealing methods

5.7. Discussion

(1) Surface morphologies and transmittance

The surface morphology of the graphene grown on the Ar annealed copper surface (Let's call it as Ar annealed graphene) has distinct characteristics. The optical images of those graphene samples (Fig. 5.1) shows three major differences from the graphene grown on the hydrogen annealed copper foil (H_2 Annealed graphene). First, the average thickness of the Ar annealed graphene is smaller than that of the hydrogen annealed graphene. Second, the distribution of multilayer regions is more irregular compare to the multilayer regions in hydrogen annealed graphene. The multilayer areas are not concentrated on the rolling lines of copper foil. In addition, the small dot-shape multilayer regions are present over the entire surface. These characteristics are due to the native copper oxide layer on the as-received copper. Since Ar is inert gas, the Ar molecules does not remove the native oxide layer. The native oxide layer in the copper surface is partially removed during the ramping and annealing steps due to the thermal reduction process. When the growth step starts, the hydrogen and methane gases completely reduce the oxide layer and form the graphene on the surface. Due to the inhomogeneous surface morphology of copper (with copper and copper oxide), the synthesized graphene also has large morphology variations. In addition, the copper oxide delays the formation of graphene and surface activation does not occur during the annealing step, which leads to the formation of thinner graphene.

The graphene synthesized on the copper that is annealed by the mixture of hydrogen and argon gas is consistent with this observation. The surface morphologies of those graphene samples (Fig. 5.2) show more regular multilayer regions that are similar to those found on the hydrogen annealed copper grown graphene. One can clearly observe the rolling line of the copper from the distribution of multilayer in these graphene samples. In addition, the synthesized graphene is thinner than for the hydrogen annealed case, when the methane flow rate is high ($CH_4/Ar = 0.005$). When the foil is annealed with a mixture of two gases, the native oxide layer on the copper is effectively removed and surface activation by the hydrogen during the annealing step is much less pronounced than that of the hydrogen only annealing case. This is because in the mixture gas annealing case, the hydrogen gas is diluted by the large argon gas flow which is inert. Therefore, the concentration of hydrogen molecules in the bulk gas flow and the boundary layer region is much lower. In this region, the copper oxide layer is efficiently removed by the hydrogen while keeping the surface activation by the hydrogen gas low.

The transmittance data present those characteristics in quantitative way. Graphene from the argon annealed copper foil has greatest transmittance over most of the methane flow rate range. The transmittance of mixture gas annealed copper foil grown graphene is higher than that of hydrogen annealed copper foil grown graphene at some points, and lower at the other points. Therefore it is hard to determine which one is superior to the other in terms of transmittance.

(2) Sheet resistance and mobility

The sheet resistance data of graphene synthesized by different annealing methods are shown in the Fig. 5.3. Interestingly the sheet resistance of the mixture gas annealed copper grown graphene is much more stable and lower than that of graphene from the two different methods. As we discussed above, the problem with argon annealing is that the annealing process cannot completely remove the native oxide layer. The remaining oxide layer leads to non-uniform graphene and introduces defects into the synthesized graphene. On the other hand, the hydrogen annealing leads to large surface activation during the initial growth step. The high surface activation results in higher nucleation density at the beginning of the growth step. Since the diluted hydrogen gas (mixture of hydrogen and argon) effectively removes native copper oxide layer while minimally activating the copper surface, the resulting graphene has lower nucleation density and shows the better sheet resistance and mobility with respect to the different methane flow rate. Raman mapping data ($CH_4/Ar = 0.005$, high methane flow rate region) of graphene synthesized by the three different annealing methods provide information about the defect density. The graphene synthesized on the argon annealed copper shows large D/G ratio over the huge area (15μm × 15μm). On the other hand, the D/G ratio of diluted hydrogen annealing methods case has some defective areas with low-defect background. Even though it has some defective region similar to the hydrogen annealed case, the lower background D/G ratio implies the lower surface activation at the beginning of the growth step.

In Fig. 5.8, the carrier mobility data of diluted hydrogen annealing case show carrier mobility that is twice as high as that of the other conditions presented in the graph. This high mobility over the different methane flow rates leads to the stable and small sheet resistance of the synthesized graphene because of the relationship between sheet resistance and mobility. This effect is especially dramatic for high methane flow rates ($CH_4/Ar > 0.003$).

Since the annealing condition is not yet optimized with respect to the hydrogen and argon flow rates, there are huge possibilities for improving the electrical and optical properties of graphene with the diluted hydrogen annealing method. In addition, combined with other growth control methods, diluted hydrogen annealing method has great potential to improve the quality of the synthesized graphene.

(3) Evaluation of the graphene quality for the transparent electrode applications

The DC-to-optical conductivity ratio data in the Fig. 5.9 provide the rough standard for the transparent conductive film. In the Fig. 5.9, the diluted hydrogen and argon annealing methods shows the similar conductivity ratios. Even though the sheet resistance of diluted hydrogen annealing copper grown graphene is lower than that of graphene from argon annealing scheme, the transmittance of argon annealing method surpasses that of diluted hydrogen annealing scheme. The compensation between the two factors causes the conductivity ratios of two methods to be similar. (But still the diluted hydrogen annealing method synthesizes the best quality graphene at high methane flow rates) The hydrogen annealed copper grown graphene shows inferior conductivity ratio for most of the methane flow region, but it presents the largest ratio at the lowest methane flow rate condition due to the huge improvement in transmittance.

In this chapter, we discussed the effect of annealing step on the material properties of resulting graphene. Hydrogen is required to completely remove the native oxide layer in the copper foil, but also activates the surface of the copper which leads to the higher nucleation density and worse electrical properties. Therefore, the annealing process with diluted hydrogen improves the quality of graphene in terms of sheet resistance and mobility. If transmittance is the most important factor for the application, argon annealing methods is a possible alternative.

In the next chapter, the author discuss about the APCVD graphene synthesis without hydrogen throughout the whole CVD process. Graphene synthesis without hydrogen is possible[10] and has the possibility of achieving good electrical and optical properties. The characterization of graphene synthesized by hydrogen-excluded process with respect to the wide range of methane flow rate will be shown in the next chapter. Also cooling step study, discussion about those synthesized graphene samples, and comparison with previous synthesis methods will be presented.

Chapter 6. Hydrogen-Excluded Graphene Synthesis

In addition to the conditions in the previous chapters that utilize the hydrogen gas during the growth step, the hydrogen-excluded graphene synthesis can produce relatively good-quality graphene. Since there is no surface activator during the CVD process, the author decided to use large methane flow (CH4/Ar > 0.01) and low argon flow (Ar = 500sccm) during the growth process. Table 6.1 shows the gas flow rates during the whole CVD process, and the table 6.2 classifies tested conditions with respect to the methane flow rate (x) during the growth step and the cooling methods. In the table 6.1, the argon flow rate during the CVD process is fixed as 500sccm. On the other hand, the methane flow rate (x) varies from condition to condition. The methane flow rate window is set as high as 80sccm to obtain single to multilayer graphene, because the very low sensitivity of graphene growth on methane flow rate was found in the preliminary study. There are two major different set of conditions with respect to the annealing method. One set of conditions has no methane flow during the cooling step, and the other set of conditions has methane flow. By comparing these two different sets of conditions, the effect of methane during the cooling step is investigated. This study focuses on the dependence of synthesized graphene on the methane flow rate and cooling step.

Gas	**I**	**II**	**III**	**IV**
CH$_4$(sccm)	**0**	**0**	$\boldsymbol{x}$	$\boldsymbol{x}$ **or 0**
Ar(sccm)	**500**	**500**	**500**	**500**

Table 6.1. The gas flow rates throughout the APCVD process

Cooling Step **CH$_4$(*sccm*)**	**Ar**	**Ar + CH$_4$**
5	O1	O2
10	P1	P2
15	Q1	Q2
40	R1	R2
60	S1	S2
80	T1	T2

Table 6.2. The conditions sorted by the cooling step and the methane flow rate during growth step

6.1. Surface Morphologies

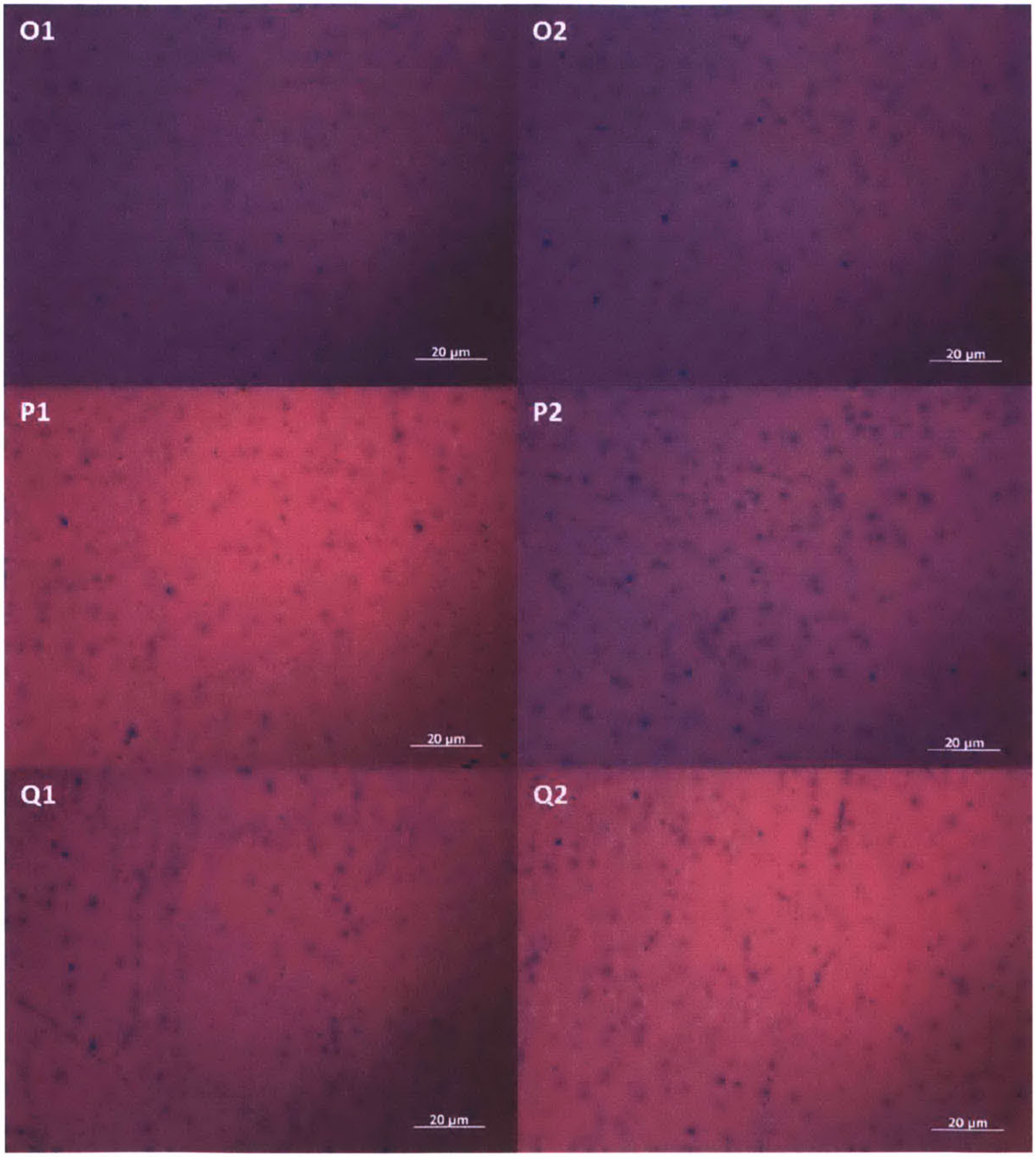

Figure 6.1. The optical microscope images of graphene samples synthesized by the hydrogen-excluded process

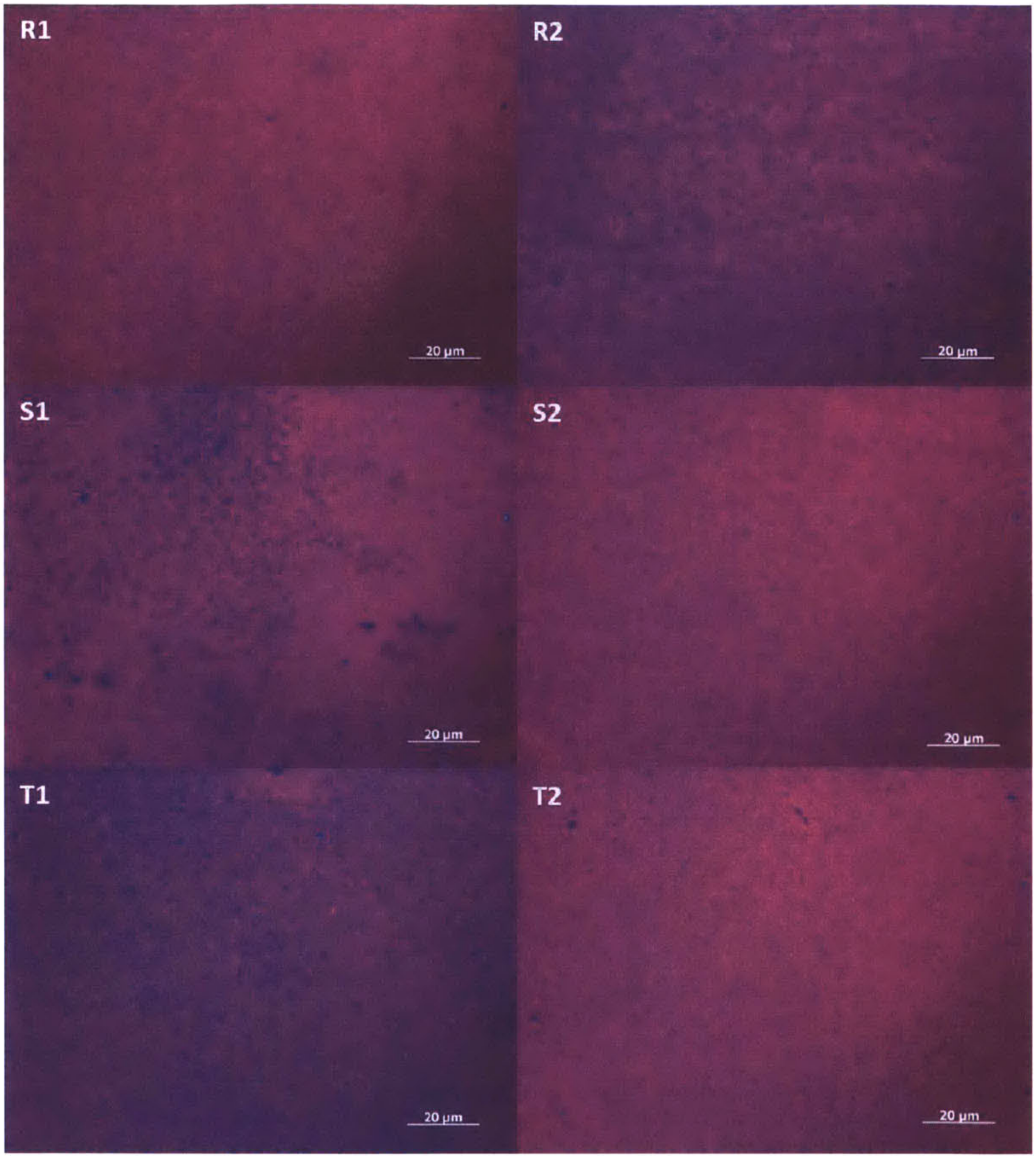

Figure 6.2. The optical microscope images of graphene samples synthesized by the hydrogen-excluded process

Fig. 6.1 and 6.2 are the optical microscope images of the graphene synthesized by the hydrogen-excluded process. The overall surface morphology is unaffected by the cooling step. One the interesting characteristic of this type of graphene is that the single layer graphene is synthesized for a wide range of methane flow rates. When the methane flow rate is lower than 15 sccm (CH4/Ar < 0.03), single layer graphene with some bilayer islands is synthesized. This is roughly 30 times lower sensitivity to methane flow rate compare to the hydrogen-assisted synthesis case.

On the other hand, when the methane flow rate is extremely high ($CH_4/Ar > 0.08$), many small dotted particles stick to the surface of the graphene. Even with higher methane flow rate, the dotted particles are created instead of multilayer graphene. Therefore this method is not suitable for multilayer graphene growth. Nonetheless, it shows relatively clean single layer graphene and thus can be utilized for the single layer graphene growth with large methane flow range.

6.2. Sheet Resistance

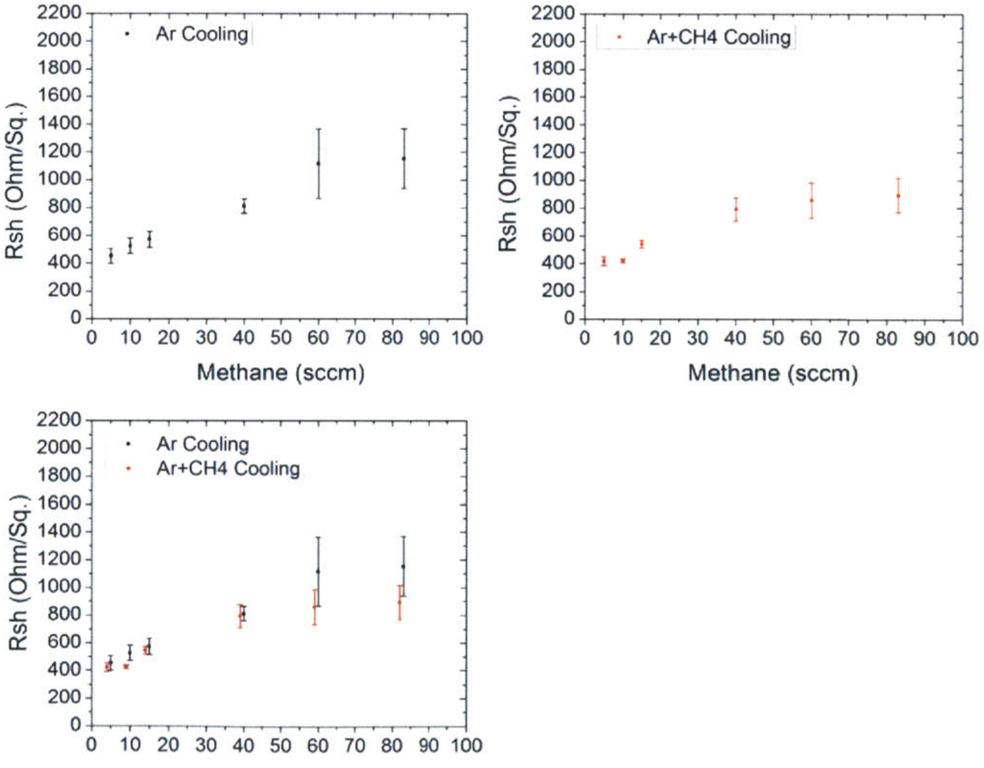

Figure 6.3. The sheet resistance vs. methane flow rate in the hydrogen-excluded synthesis method

Fig. 6.3 shows the sheet resistance data of the graphene from the hydrogen-excluded synthesis method. According to these data, the sheet resistance linearly increases (with an offset) as the methane flow rate rises, and saturates to some constant value for high methane flow rates. Once again, there is no significant difference between the sheet resistances of the graphene from methane-excluded cooling and methane-included cooling steps. There is some discernible difference only when the methane flow rate is extremely large ($CH_4/Ar > 0.12$).

6.3. Transmittance

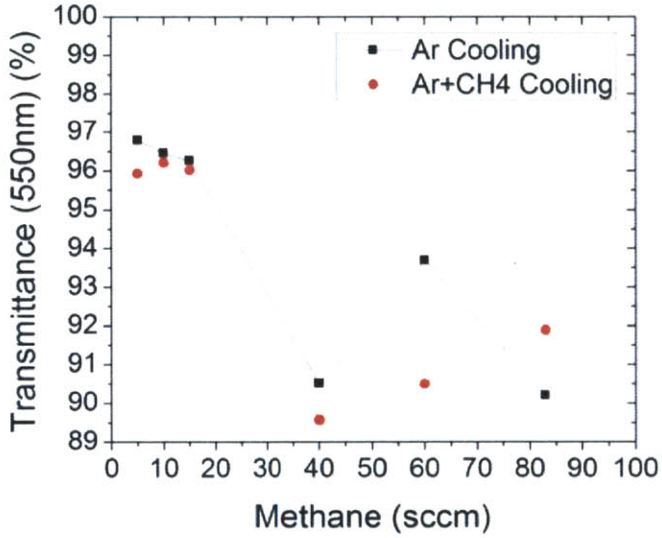

Figure 6.4. The transmittance vs. methane flow rate

Fig. 6.4 presents the transmittance data with respect to the methane flow rate. At relatively low methane flow rates ($CH_4/Ar < 0.03$, This value is still pretty high for the hydrogen assisted graphene synthesis), the synthesized graphene sample shows transmittances larger than 95.9% which is corresponds to single layer graphene with bilayer islands. In the extremely high methane flow rate region ($CH_4/Ar > 0.08$), the transmittance shows no clear trend. The only thing the author can confirm is that the transmittance of this range of methane flow rate is lower than that of the relatively low methane flow rate region. The last observation is that even though it was difficult to tell from the optical microscope images, the transmittance of methane excluded cooled graphene is slightly higher than that of methane included cooled graphene.

6.4. Carrier Mobility

Fig. 6.5~6.7 are the carrier mobility and carrier concentration data of the graphene synthesized by the hydrogen-excluded synthesis process. Both methane excluded and included cooling methods show nearly identical carrier mobility values. Different from the sheet resistance trend, the carrier mobility has negative correlation with methane flow rate. Carrier mobility decreases (with some offset), and saturates to $450(\mathrm{cm}^2/\mathrm{V \cdot s})$ in the extremely high methane flow rate region ($CH_4/Ar > 0.08$). If we decrease methane flow rate, the mobility increases to $1393(\mathrm{cm}^2/\mathrm{V \cdot s})$ which is a relatively high value. Further improvement in carrier mobility could be realized by further decreasing methane flow rate.

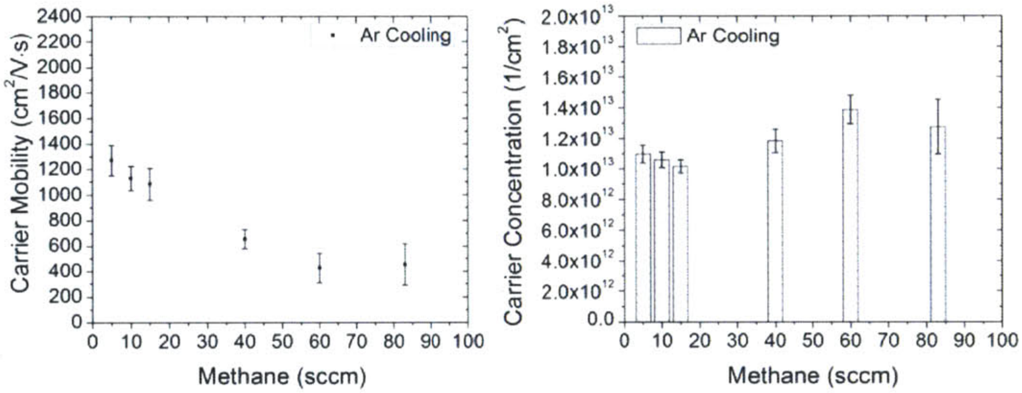

Figure 6.5. Carrier mobility and carrier concentration data of the graphene synthesized by the hydrogen-excluded synthesis and methane excluded process

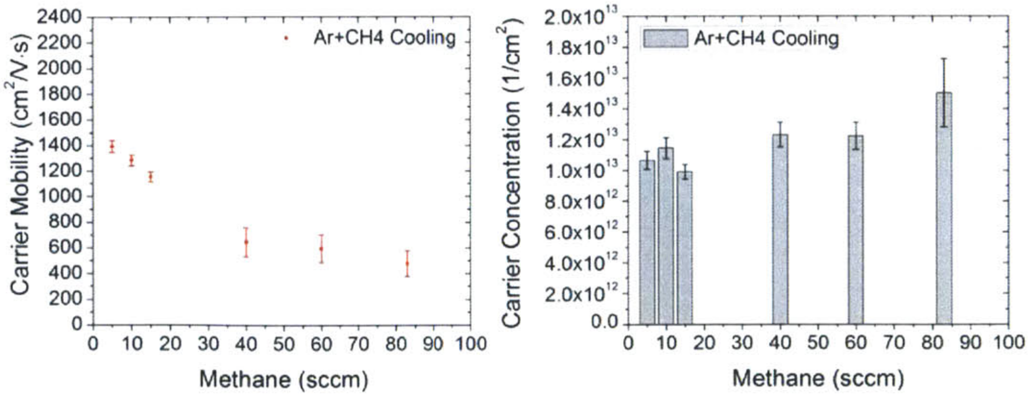

Figure 6.6. Carrier mobility and carrier concentration data of the graphene synthesized by the hydrogen-excluded synthesis and methane included process

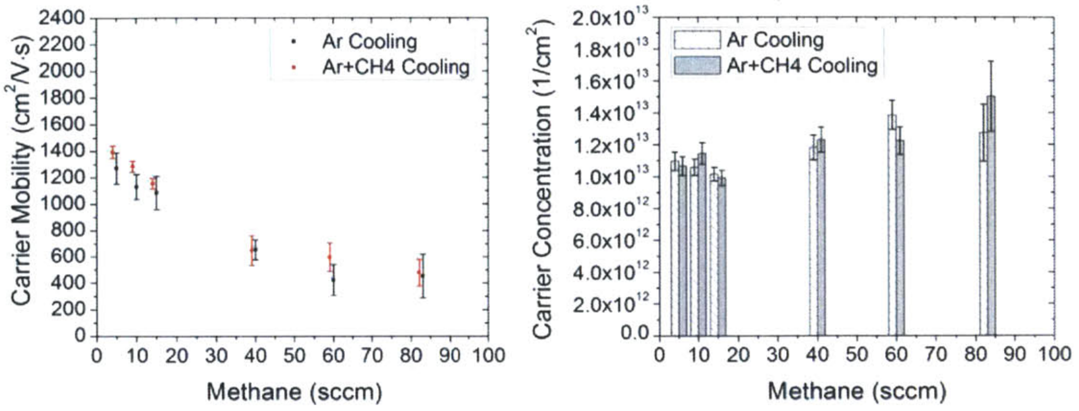

Figure 6.7. Carrier mobility and carrier concentration data of the graphene synthesized by the hydrogen-excluded process

6.5. Quality of graphene synthesized by Hydrogen-excluded process

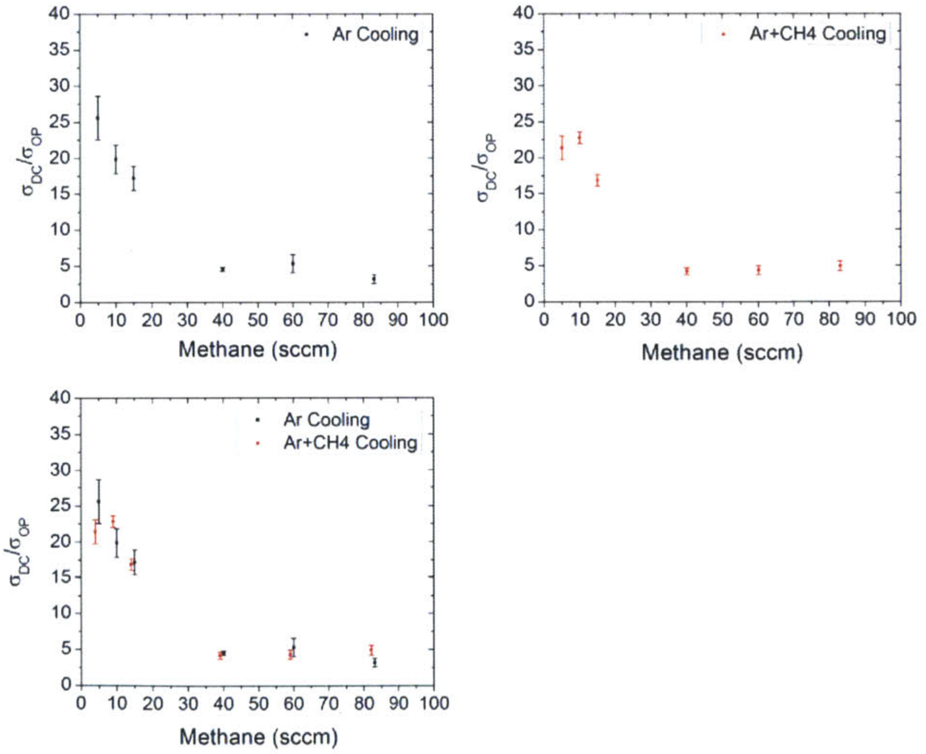

Figure 6.8. The DC to optical conductivity ratio of the graphene synthesized by the hydrogen-excluded process

The DC to optical conductivity ratio data in Fig. 6.8 shows negative correlation with the methane flow rate, as expected. Throughout the whole report, it is a global trend that lower methane flow rate during the growth step results in higher overall quality of synthesized graphene. The ratio values are high except the graphene synthesized at the extremely high methane flow rates ($CH_4/Ar > 0.08$). This is partially due to the dotted particles which are detrimental to transmittance, and do not help the sheet resistance.

6.6. Discussion

(1) Surface morphology and transmittance

One of the most distinctive features of the graphene synthesized without hydrogen is that single layer graphene with low bilayer islands is created at high methane flow rates. The methane to argon flow rate ratio ($CH_4/Ar > 0.01$) is at least two times larger than that of previous conditions. Even for very large methane flow rates ($CH_4/Ar = 0.03$), single layer graphene is synthesized. Since there is no surface activator to enhance the creation of active carbon species for the formation of graphene, the hydrogen-excluded process allows for a wide range of methane flow rate for single layer graphene synthesis. The author increased methane flow rate further up to the 83sccm to synthesize multilayer graphene ($CH_4/Ar = 0.166$). For the extremely high methane flow rate case ($CH_4/Ar > 0.08$), amorphous carbon is formed on top of the single layer surface. Due to the large amount of carbon source and the absence of etching reagent, the amorphous carbon is created and sticks to the monolayer background rather than being etched away. Because amorphous carbon is created rather than the multilayer graphene, the hydrogen-excluded CVD process is not suitable for the multilayer graphene synthesis. It is more useful to synthesize single layer graphene with large methane window.

The transmittance data in the Fig. 6.4 presents more quantitative trend which is consistent with the observation above. At the relatively lower methane flow rate region ($CH_4/Ar < 0.03$, it is still much higher than previous conditions), the transmittance is consistent with the single layer graphene with bilayer islands. At the extremely high methane flow rate region ($CH_4/Ar > 0.08$), there is almost no trend in the transmittance data. In this region, the amount of amorphous carbon sticking to the graphene surface determines transmittance. The amorphous carbon could be removed during the post annealing process, which is independent of the growth condition.

Therefore the transmittance in the extremely high methane flow rate region does not show any trend.

Transmittance data also shows the small difference between argon cooling and argon + methane cooling conditions. Since the methane flow during the cooling step protects the graphene from the dissociation, the transmittance of graphene synthesized with the methane included cooling process is lower than that of graphene grown with methane-less cooling step.

(2) Sheet resistance and mobility

Similar to the previous observation, the sheet resistance of hydrogen-excluded graphene (graphene synthesized by the hydrogen-excluded process) increases as the methane flow rate rises. This is because the higher methane flow rate enhances nucleation of the graphene. Higher nucleation density results in the more domain boundary scattering over the graphene sheet that leads to the smaller mobility and higher sheet resistance. The reason is same as for the methane controlled single-to-multilayer graphene case. However, the size of methane flow range for hydrogen-excluded graphene is roughly 24 times larger than that of the methane controlled graphene. This is due to the absence of a surface activator. On the other hand, the sheet resistance of the graphene with methane included cooling step is slightly lower than that of the graphene with argon-only cooling step. The methane flow during the cooling step protects the graphene layer from the dissociation and leads to the better sheet resistance. The sheet resistance reaches 422 (Ω/□) when the methane flow rate decreases to 5 sccm (CH_4/Ar: 0.01).

The mobility data in Fig. 6.7 is consistent with the sheet resistance data discussed above. Carrier mobility decreases as the methane flow rate increases due to larger nucleation density. Once again the graphene with methane-included cooling step shows slightly higher carrier mobility.

(3) Evaluation of the graphene with for transparent electrode applications

The hydrogen-excluded graphene samples have relatively high DC-to-optical conductivity ratios for the wide range of the methane flow rates. This series of graphene samples have high transmittance values due to the monolayer dominated morphologies, which results in high conductivity ratios. When the methane flow rate is lower than 15 sccm ($CH_4/Ar < 0.03$), the DC-to-optical conductivity ratio is higher than 16.8 which is much higher than 11. On the other hand, the DC-to-optical conductivity ratios of two different series of graphene (synthesized with methane included cooling step/argon only cooling step) do not show distinctive differences. This is because there is trade-off between the transmittance and sheet resistance in these cases.

Throughout this chapter, graphene synthesis without hydrogen was been studied with respect to methane flow rate and the cooling step. Hydrogen-excluded graphene synthesis has advantages when it comes to the single layer graphene synthesis with relatively high quality. The process is not sensitive to the methane flow rate, and creates good single layer graphene with small bilayer island density. However, this process cannot be utilized to synthesize multilayer graphene due to the creation of amorphous carbon rather than multilayer graphene. Also, the mobility and the sheet resistance are not as good as with hydrogen-controlled or annealing step-tuned graphene. Therefore, this type of graphene is suited for low cost synthesis of relatively high-quality monolayer graphene.

Chapter 7. Conclusions

(1) Methane Controlled Single-to-Multilayer Graphene Synthesis

Synthesis of single-to-multilayer graphene is possible by varying the methane flow rate during the growth step. When hydrogen flow rate is in the low to moderate range ($H_2/Ar \leq 0.01$), fewer multilayer regions are created when methane flow rate is lowered. The concentration of active carbon species is directly related to the methane flow rate, which determines the reaction rate on the copper's surface. Therefore, single layer graphene synthesis with low methane flow rate ($CH_4/Ar < 0.0004$), and multilayer graphene synthesis with high methane flow rate ($CH_4/Ar > 0.0035$) are readily achievable. However, there is a problem in utilizing high methane flow rate condition for multilayer graphene synthesis: high methane flow is detrimental to the film's electrical and optical properties. As methane flow rate rises, the sheet resistance increases, and the carrier mobility and the transmittance decrease. Since high methane flow rate introduces more defects per unit area, high quality multilayer graphene cannot be synthesized by the methane control method. On the other hand, relatively high quality single layer graphene synthesis is possible with this method using diluted methane gas.

(2) Hydrogen Controlled Single-to-Multilayer Graphene Synthesis

To compliment methane controlled multilayer graphene synthesis, hydrogen controlled methods were studied. Since hydrogen acts as a surface activator, growth rate control can be achieved by tuning hydrogen flow. Diluted methane (100ppm in Ar) was used to ensure that the sheet resistance of the synthesized graphene was as low as possible, as concluded in Chapter 2. Consistent with this understanding, the synthesized graphene shows low sheet resistance, high mobility and very low D/G ratio for a large hydrogen flow window (H_2/Ar: 0.0012~0.060). On the other hand, mono ($H_2/Ar = 0.0012$) to multilayer ($H_2/Ar = 0.040$) graphene was synthesized by the controlling the hydrogen flow rate. When the hydrogen flow rate is low ($H_2/Ar < 0.005$), the copper surface is not well activated, but reaches the full activation stage as the hydrogen flow rate rises ($H_2/Ar > 0.040$). Therefore, the average number of graphene layer depends on the hydrogen flow rate. Besides, the electrical properties are related to the domain size of the graphene in hydrogen controlled graphene synthesis (Due to the low defect density). If hydrogen flow rate is lower than certain point ($H2/Ar < 0.080$), the sheet resistance decreases and mobility increases as hydrogen flow rate rises. This is due to the negative correlation between nucleation density and hydrogen flow rate. Overall, the hydrogen control method has advantages over the methane control method. Hydrogen control method is able to achieve multilayer graphene with much less detrimental effects on its quality than the methane control method.

(3) Graphene Synthesis by Growth Temperature Engineered Process

Growth temperature engineering was done to further improve the quality of graphene. Due to the high desorption rate of active carbon species, the lower nucleation density is achievable with higher growth temperatures. In this study, the single layer graphene condition ($H_2/Ar = 0.005$, with 100ppm diluted methane) from chapter 3 was used. Three different growth temperatures (1000°C, 1035°C, 1070°C) were studied. When the temperature rises from 1000°C to 1035°C, the material properties of graphene do not change significantly. However, the graphene synthesized at 1070°C exhibits enhanced electrical and optical properties. The synthesized graphene showed sheet resistance of 331.42($\Omega/\square$), transmittance of 96.93(%),mobility of 2038.95($\mathrm{cm}^2/\mathrm{V}\cdot\mathrm{s}$), and DC-to-optical conductivity ratio of 36.22. Therefore, tuning the growth temperature allows for the synthesis of the highest quality graphene. However, increasing growth temperature adjustment also increases the cost of synthesis as higher furnace temperature is required.

(4) Graphene Synthesis by Annealing Step Engineered Process

In this study, three different annealing (step II of Fig.A.1) methods were tested: hydrogen annealing, argon annealing, and diluted hydrogen annealing. The graphene synthesized using the argon annealing method shows similar properties as the graphene grown with the hydrogen annealing method except that the argon annealing method results in higher transmittance. On the other hand, the diluted hydrogen (hydrogen gas diluted by argon gas) annealing method produces graphene with superior electrical properties over different methane flow rates. This is due to the adjusted activation level of the copper foil. In the hydrogen annealing case, the copper foil is highly activated by the high concentration of hydrogen gas during the ramping and annealing steps. Thus, when the methane gas is introduced, many nucleation sites are created which leads to worse electrical properties. On the other hand, in the argon annealing case, the native copper oxide cannot be fully eliminated during the annealing step which results in low quality graphene. The diluted hydrogen annealing method combines the advantages of each method. With some hydrogen molecules in the gas mixture, the native oxide can be eliminated. In addition, the surface is less activated than with pure hydrogen, thus, fewer nucleation sites are created at the beginning of the growth step. Since the diluted hydrogen annealing method results in very high mobility and low sheet resistance for a relatively large methane flow window, it can be utilized to synthesize high quality graphene. Also, relatively high quality multilayer graphene synthesis is possible with this method.

(5) Hydrogen Excluded Graphene Synthesis

In chapter 6, graphene synthesis without hydrogen was studied. Since this method does not introduce hydrogen gas throughout the process, it has a wide methane flow window. Similar to previous discussions, the electrical and optical properties are degraded as methane flow rate increases, due to the high concentration of active carbon species. The effect of methane during the cooling step was also studied. Even though the graphene from methane included cooling exhibits slightly better transmittance and worse electrical properties, the differences are not statistically significant. Relatively high quality single layer graphene is readily producible with this method ($CH_4/Ar < 0.03$), due to its insensitivity to the methane flow rate. However, when the methane flow rate is extremely high ($CH_4/Ar > 0.08$), dotted particles are created rather than multilayer graphene. Therefore this method is not suitable for multilayer graphene synthesis. A comparison of these five synthesis methods is presented in table 7.1 and 7.2.

Synthesis Methods	**Advantages**	**Disadvantages**	**Potentials**
Methane Controlled Single-to-Multilayer Graphene	1) Multilayer graphene is readily available 2) Relatively high quality single layer graphene synthesis is possible	1) Material properties are highly sensitive to the methane flow rate 2) Multilayer graphene has high defect density	1) Thick multilayer graphene synthesis 2) Relatively high quality single layer graphene synthesis
Hydrogen Controlled Single-to-Multilayer Graphene	1) Low defect density for large hydrogen window (w/ low methane flow rate) 2) High quality multilayer graphene synthesis is possible	1) The effect of hydrogen is complicated	1) High quality multilayer graphene synthesis 2) High quality single layer graphene synthesis
Growth Temperature Engineered Graphene	1) Provides the highest electronic and optical properties	1) Cost rises due to the high growth temperature	1) Highest quality graphene synthesis
Annealing Step Engineered Graphene	1) High carrier mobility (Diluted Hydrogen Annealing Case) 2) Good electronic properties are maintained for relatively wide methane window (Diluted Hydrogen Annealing Case)		1) High carrier mobility required applications 2) The process could be applied to other synthesis methods
Graphene synthesized by Hydrogen-Excluded Process	1) Single layer graphene synthesis is possible for very wide methane window	1) Multilayer graphene synthesis is hard to achieve	1) Single layer graphene with relatively high quality is readily available

Table 7.1. Summary of the five different APCVD synthesis methods studied in this thesis

Synthesis Methods	Best Sheet Resistance **($\Omega/\square$)**	Highest Transmittance (550nm) **(%)**	Highest Carrier Mobility **($cm^2/V \cdot s$)**	Best **σ_{DC}/σ_{OP}**
Methane Controlled Single-to-Multilayer Graphene	**366.58** (1.32×10^{13} cm^{-2})	**96.97**	**1484.21** (1.01×10^{13} cm^{-2})	**33.12**
Hydrogen Controlled Single-to-Multilayer Graphene	**372.01** (8.07×10^{12} cm^{-2})	**96.87**	**2086.38** (8.07×10^{12} cm^{-2})	**28.53**
Growth Temperature Engineered Graphene	**331.42** (9.29×10^{12} cm^{-2})	**96.93**	**2038.95** (9.29×10^{12} cm^{-2})	**36.22**
Annealing Step Engineered Graphene	**347.08** (9.19×10^{12} cm^{-2})	**95.91**	**1960.13** (9.19×10^{12} cm^{-2})	**21.86**
Graphene synthesized by Hydrogen-Excluded Process	**422.02** (1.07×10^{13} cm^{-2})	**96.79**	**1393.05** (1.07×10^{13} cm^{-2})	**25.29**

Table 7.2. The Best Electronic and Optical Properties of Graphene Synthesized by Each Method

Future Works

1. Photovoltaic Device Fabrication

The synthesis conditions that resulted in the best quality Single-to-Multilayer graphene were found in this study. Remaining work includes fabricating photovoltaic devices using the best graphene samples. Single and multilayer APCVD, and LPCVD graphene samples will be patterned as transparent electrodes for OPVs. As we discussed in the previous chapters, multilayer graphene could be better a option compared to monolayer graphene due to its mechanical robustness. The performances of devices that are composed of single-to-multilayer graphene samples will be measured and compared. OPVs with one to four layers of graphene as transparent electrodes will also be fabricated to set the standard. The goals of this study are shown below.

(1) Demonstrate high performance APCVD graphene electrode OPVs.

(2) Determine the best APCVD graphene synthesis condition for transparent electrodes.

2. Investigation over the relationship between material properties of graphene and the number of layers

To obtain low sheet resistance (~30Ω/□ with doping) and relatively high transmittance (> 90%), stack of 3~4 layers of graphene is required. As the number of graphene layers increases, transmittance decreases linearly. However, dependences of mobility and sheet resistance on the number of stacked graphene layers are still not understood. From the experimental results, it is true that sheet resistance decreases as the number of layers increases.[31] Carriers can move either along the plane, or out of plane, which leads to lower sheet resistance. By building up the model which describes the phenomena, the effects of multilayers on electrical properties will become much clearer. Also, this model can be extended to the discontinuous multilayer case, to figure out the contribution of multilayer islands over the electrical properties of graphene.

Appendices

Method

1. APCVD Synthesis

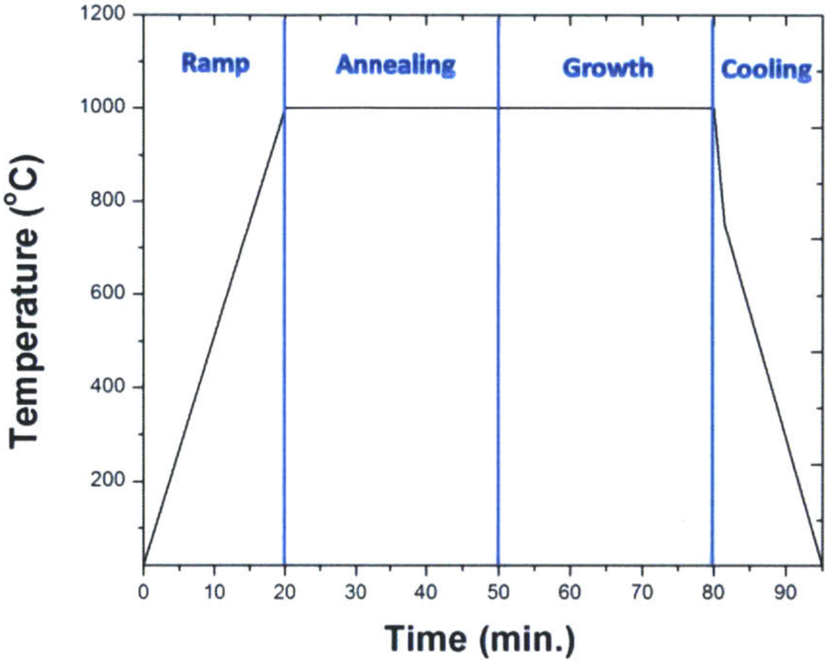

Figure A. 1. The temperature of the quartz tube during the synthesis process

(1) Prepare the $1 \times 2.5\ \mathrm{inch}^2$ copper foil (99.8%, $25\mu\mathrm{m}$, Alfa Aesar)

(2) Blow the copper foil with the blowgun to get rid of possible dust particles on the copper (use the clean blowgun)

(3) Place the prepared copper foil in the quartz tube.

(4) Purge out the air in the tube and place the tube in the furnace.

(5) Heat up the furnace and operate it according to the temperature vs. time plot in Fig. A.1.

(6) Open the furnace when the cooling step starts for the rapid cooling.

2. Graphene Transfer

(1) Cut and sonicate PET film in the DI water.

(2) Tape the four edges of the copper foil (with graphene) onto the PET film.

(3) Spin coat 4.5 wt% PMMA solution (MicroChem, 950,000 MW, dissolved in anisole) on the taped copper foil

(4) Bake the coated copper foil at 70°C for 20 min in the oven.

(5) Cut the edges of baked copper foil to get rid of PET film.

(6) Etch away the copper foil in commercial copper etchant ($FeCl_3$ solution) for 1 hour.

(7) Rinse the graphene with DI water.

(8) Get rid of ions and chemicals with 10 wt% HCl solution for 30 minutes.

(9) Rinse graphene with DI water

(10) Clean Si/SiO_2 substrates and transfer PMMA/graphene film on top of the substrate.

(11) Blow-dry PMMA/graphene with blowgun to get rid of water between the graphene and the SiO_2.

(12) Anneal the transferred sample with 700sccm of hydrogen and 400sccm of argon.

3. Hall Effect Measurement

(1) Make indium contacts on four corners of graphene sample.

(2) With home-made 4 tip probe, measure the sheet resistance of the sample.

(3) Place a magnet (2000 gauss) beneath the sample and measure the hall voltage.

(4) Extract carrier concentration from the hall voltage.

(5) Get carrier mobility from sheet resistance and carrier concentration values.

4. Transmittance

(1) Transfer graphene onto borosilicate glass substrate.

(2) Place a bare glass substrate in the sample holder and set the reference of UV-Vis (Cary 5000) as 100%.

(3) Block the light that goes to the detector and set the reference as 0%.

(4) Put the sample with graphene in the sample holder and measure transmittance.

5. Raman

(1) Turn on the laser (532nm, 0.1W) and place the sample on the microscope.

(2) Focus on sample with white light

(3) Set focus time to 4 seconds, and acquire time to 4 seconds

(4) Focus the laser on the sample, and acquire Raman signal

(5) Set the scanning range and the number of pixels.

(6) Get Raman mapping data.

(7) Process Raman mapping data and extract D/G and G'/G ratios.

Bibliographic References

---

[1] Xuan Wang, Linjie Zhi, and Klaus Mullen, Transparent, Conductive Graphene Electrodes for Dye-Sensitized Solar Cells, NANO LETTERS, 2008, Vol. 8, No. 1, 323-327

[2] Junbo Wu, Héctor A. Becerril, Zhenan Bao, Zunfeng Liu, Yongsheng Chen, and Peter Peumans, Organic solar cells with solution-processed graphene transparent electrodes, Appl. Phys. Lett. 92, 263302 (2008)

[3] Vincent C. Tung, Li-Min Chen, Matthew J. Allen, Jonathan K. Wassei, Kurt Nelson, Richard B. Kaner, and Yang Yang, Low-Temperature Solution Processing of Graphene-Carbon Nanotube Hybrid Materials for High-Performance Transparent Conductors, NANO LETTERS, 2009, Vol. 9, No. 5, 1949-1955

[4] Jen-Hsien Huang, Jheng-Hao Fang, Chung-Chun Liu, and Chih-Wei Chu, Effective Work Function Modulation of Graphene/Carbon Nanotube Composite Films As Transparent Cathodes for Organic Optoelectronics, ACS Nano, VOL. 5, NO. 8, 6262–6271, 2011

[5] Minhyeok Choe, Byoung Hoon Lee, Gunho Jo, June Park, Woojin Park, Sangchul Lee, Woong-Ki Hong, Maeng-Je Seong, Yung Ho Kahng, Kwanghee Lee, Takhee Lee, Efficient bulk-heterojunction photovoltaic cells with transparent multi-layer graphene electrodes, Organic Electronics, 11, (2010), 1864–1869

[6] Xiaochang Miao, Sefaattin Tongay, Maureen K. Petterson, Kara Berke, Andrew G. Rinzler, Bill R. Appleton, and Arthur F. Hebard, High Efficiency Graphene Solar Cells by Chemical Doping, Nano Letters, 2012

[7] Tae-Hee Han, Youngbin Lee, Mi-Ri Choi, Seong-Hoon Woo, Sang-Hoon Bae, Byung Hee Hong, Jong-Hyun Ahn and Tae-Woo Lee, Extremely efficient flexible organic light-emitting diodes with modified graphene anode, NATURE PHOTONICS, VOL 6, FEBRUARY 2012

[8] Sukang Bae, Hyeongkeun Kim, Youngbin Lee, Xiangfan Xu, Jae-Sung Park, Yi Zheng, Jayakumar Balakrishnan, Tian Lei, Hye Ri Kim, Young Il Song, Young-Jin Kim, Kwang S. Kim, Barbaros O¨ zyilmaz, Jong-Hyun Ahn, Byung Hee Hong and Sumio Iijima, Roll-to-roll production of 30-inch graphene films for transparent electrodes, NATURE NANOTECHNOLOGY, VOL 5, AUGUST, 2010, 574

[9] Sreekar Bhaviripudi, Xiaoting Jia, Mildred S. Dresselhaus, and Jing Kong, Role of Kinetic Factors in Chemical Vapor Deposition Synthesis of Uniform Large Area Graphene Using Copper Catalyst, Nano Lett, 2010, 10, 4128–4133

[10] Libo Gao, Wencai Ren, Jinping Zhao, Lai-Peng Ma, Zongping Chen, and Hui-Ming Cheng, Efficient growth of high-quality graphene films on Cu foils by ambient pressure chemical vapor deposition, Appl. Phys. Lett. 97, 183109 (2010)

[11] Ivan Vlassiouk, Murari Regmi, Pasquale Fulvio, Sheng Dai, Panos Datskos, Gyula Eres, and Sergei Smirnov, Role of Hydrogen in Chemical Vapor Deposition Growth of Large Single-Crystal Graphene, ACS Nano, VOL. 5, NO. 7, 6069–6076, 2011

[12] Hui Bi, Fuqiang Huang, Jun Liang, Yufeng Tang, Xujie Lu, Xiaoming Xie and Mianheng Jiang, Large-scale preparation of highly conductive three dimensional graphene and its applications in CdTe solar cells, J. Mater. Chem., 2011, 21, 17366

[13] Alfonso Reina, Xiaoting Jia, John Ho, Daniel Nezich, Hyungbin Son, Vladimir Bulovic, Mildred S. Dresselhaus, and Jing Kong, Large Area, Few-Layer Graphene Films on Arbitrary Substrates by Chemical Vapor Deposition, Nano Lett., Vol. 9, No. 1, 2009

[14] Sukanta De and Jonathan N. Coleman, Are There Fundamental Limitations on the Sheet Resistance and Transmittance of Thin Graphene Films?, ACS Nano, VOL. 4, NO. 5, 2713–2720, 2010

[15] Wenhua Zhang, Ping Wu, Zhenyu Li, and Jinlong Yang, First-Principles Thermodynamics of Graphene Growth on Cu Surfaces, J. Phys. Chem. C, 2011, 115, 17782–17787

[16] Cecilia Mattevi, Hokwon Kima, Manish Chhowalla, A review of chemical vapour deposition of graphene on copper, J. Mater. Chem., 2011, 21, 3324–3334

[17] Siegfried Eigler, A new parameter based on graphene for characterizing transparent, conductive materials, Carbon, 47 (12), 2936–2939, 2009

[18] Xuesong Li, Carl W. Magnuson, Archana Venugopal, Jinho An, Ji Won Suk, Boyang Han, Mark Borysiak, Weiwei Cai, Aruna Velamakanni, Yanwu Zhu, Lianfeng Fu, Eric M. Vogel, Edgar Voelkl, Luigi Colombo, and Rodney S. Ruoff, Graphene Films with Large Domain Size by a Two-Step Chemical Vapor Deposition Process, Nano Lett., 2010, 10 (11), 4328–4334

[19] Dechao Geng, Bin Wu, Yunlong Guo, Liping Huang, Yunzhou Xue, Jianyi Chen, Gui Yu, Lang Jiang, Wenping Hu, and Yunqi Liu, Uniform hexagonal graphene flakes and films grown on liquid copper surface, PNAS, 2012

[20] Yimin A. Wu, Ye Fan, Susannah Speller, Graham L. Creeth, Jerzy T. Sadowski, Kuang He, Alex W. Robertson, Christopher S. Allen, and Jamie H. Warner, Large Single Crystals of Graphene on Melted Copper Using Chemical Vapor Deposition, ACS Nano, 2012

[21] Cathleen Thiele and Raghu Das, Markets, Transparent Conductive Films 2012-2022: Technologies and Assessment of ITO's Future and its Alternatives, IDTechEx, 2012

[22] Phaedon Avouris, Graphene: Electronic and Photonic Properties and Devices, Nano Lett. 2010, 10, 4285–4294

[23] Lewis Gomez De Arco, Yi Zhang, Cody W. Schlenker, Koungmin Ryu, Mark E. Thompson, and Chongwu Zhou, Continuous, Highly Flexible, and Transparent Graphene Films by Chemical Vapor Deposition for Organic Photovoltaics, ACS Nano, VOL 4, NO. 5, 2865–2873, 2010

[24] Xiangjian Wan, Guankui Long, Lu Huang, and Yongsheng Chen, Graphene – A Promising Material for Organic Photovoltaic Cells, Adv. Mater. 2011, 23, 5342–5358

[25] Shengrui Sun, Lian Gao, and Yangqiao Liu, Enhanced dye-sensitized solar cell using graphene-TiO2 photoanode prepared by heterogeneous coagulation, APPLIED PHYSICS LETTERS, 96, 083113, 2010

[26] Hyesung Park, Patrick R. Brown, Vladimir Bulović, and Jing Kong, Graphene As Transparent Conducting Electrodes in Organic Photovoltaics: Studies in Graphene Morphology, Hole Transporting Layers, and Counter Electrodes, Nano Lett, 2011

[27] P. P. Edwards, A. Porch, M. O. Jones, D. V. Morgan and R. M. Perks, Basic materials physics of transparent conducting oxides, Dalton Trans., 2004, 2995–3002

[28] A. K. Geim, and K. S. Novoselov, The rise of graphene, Nature Materials **6**, 183 - 191 (2007)

[29] F. Bonaccorso, Z. Sun, T. Hasan and A. C. Ferrari, Graphene photonics and optoelectronics, Nature Photonics **4**, 611 - 622 (2010)

[30] Yu Wang, Shi Wun Tong, Xiang Fan Xu, Barbaros Özyilmaz, and Kian Ping Loh, Interface Engineering of Layer-by-Layer Stacked Graphene Anodes for High-Performance Organic Solar Cells, Adv. Mater. 2011, 23, 1514–1518

[31] Xuesong Li, Yanwu Zhu, Weiwei Cai, Mark Borysiak, Boyang Han, David Chen, Richard D. Piner, Luigi Colombo, and Rodney S. Ruoff, Transfer of Large-Area Graphene Films for High-Performance Transparent Conductive Electrodes, Nano Lett., Vol. 9, No. 12, 2009